Investigation of the microstructural distribution in a trailing arm made of silicon-containing spring steel

Submitted by

Angeliki Tzelepi

In fulfilment of the requirements for the degree of

MSc in Materials Science and Engineering

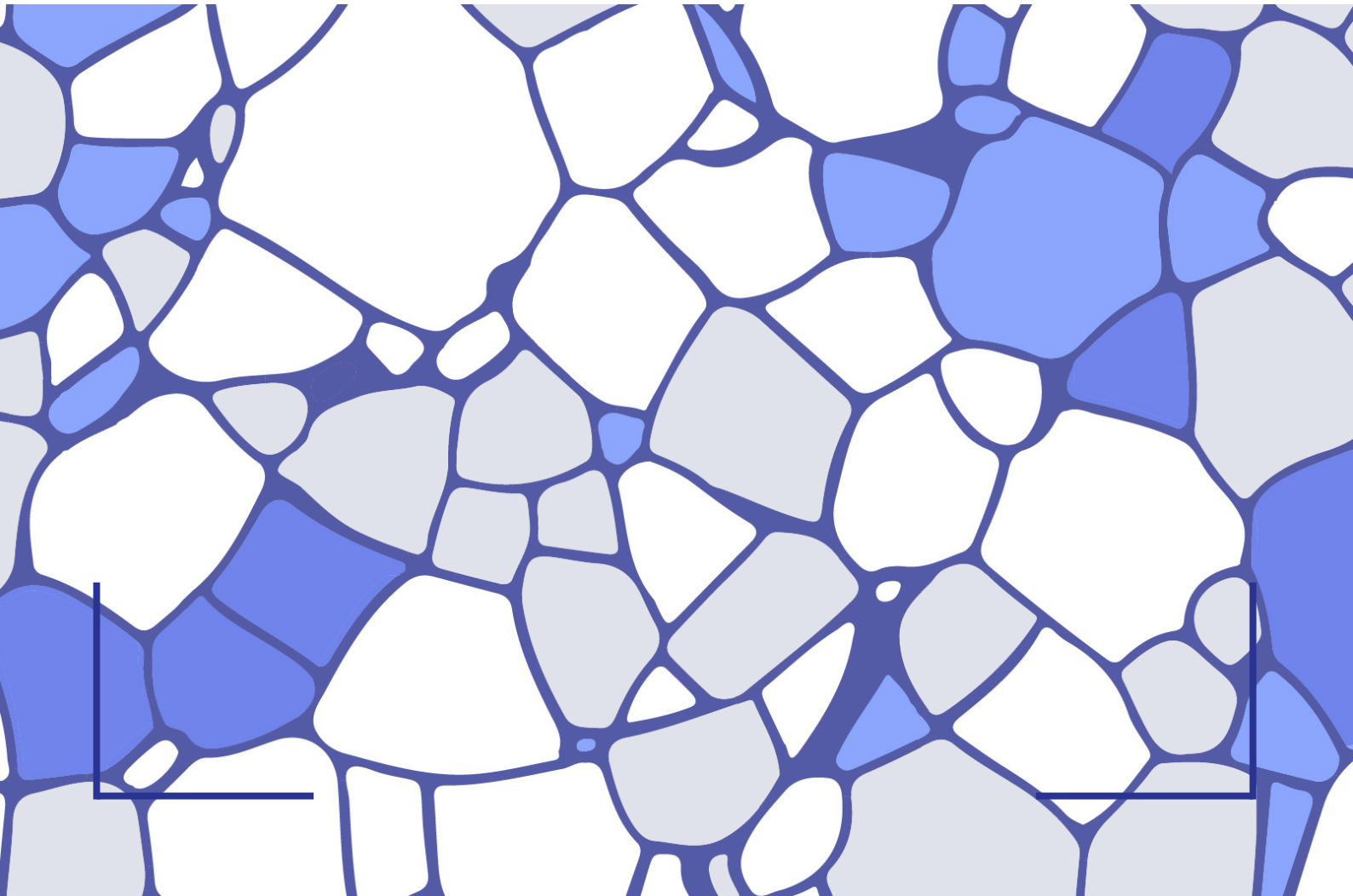

Master thesis
Department of Materials Science & Engineering
Faculty of Mechanical, Maritime and Materials Engineering

Author: **Angeliki Tzelepi**
Student number: 5364019

Thesis Committee:
Prof.Dr. Maria J.Santofimia Navarro
Dr. L. Zhao (VDL Weweler)
Prof.dr.ir. J. Sietsma
Dr. P. Dey

To be defended publicly on December 19th 2022 at 11:00.
Delft University of Technlogy
Delft, The Netherlands

An electronic version of this thesis is available at:
https://repository.tudelft.nl/

TU Delft VDL Weweler

ACKNOWLEDGEMENTS

Firstly, I would like to express my deep gratitude to Prof. dr. Maria J. Santofimia Navarro not only for her guidance and advice during this project but also, for giving me the chance to deepen my knowledge in materials science. Thank you for your patience and for handling my habit of rushing into things.

Furthermore, I would like to thank Dr. Lie Zhao for his help, and guidance and for giving me the chance to deal with a real industry issue.

I would also like to thank Ing. Kees Kwakernaak for his help with microstructure analysis using EPMA and instructions on using SEM. I am also thankful to Ing. Ruud Hendrikx and Ing. Richard Huizenga for helping me with XRD measurements and Thermocalc software. Furthermore, I would also like to acknowledge the technicians of the Department of Materials Science and Engineering of the Delft University of Technology. Many thanks to Remko Seijffers and student assistants: Seizen Kadir, Alice Dautezac, and Thanasis Kefalas, for helping me during sample preparation.

I would also like to thank my boyfriend Chris, all my friends in the Netherlands (Dionysis, Efthymis, and Thanasis), and especially my architect friends (Faidra, Ioanna, Katerina, and Leto) for making this study period special and helping me with graphs. Special thanks also to my friends that were back in Greece (Jenny, Simela, Vicky, Iro), but they always supported me.

Last but not least, I would like to thank my parents and brother for their endless and unconditional support during my academic life; nothing would have been possible without them.

ABSTRACT

The presence of bainite and retained austenite in advanced high-strength steels (AHSS) has grown a great interest in the automotive industry as simultaneously provides strength and the transformation-induced plasticity (TRIP) effect. This type of microstructure is present in modern trailing arms. A trailing arm is part of the air suspension system in heavy vehicles. In spring steels, such as the ones used to produce trailing arms, this combination of bainite and retained austenite is obtained by a heat treatment named austempering.

In this work, the microstructural distribution of a silicon spring steel (Fe-0.6C-1.63Si-0.97Mn-0.48Cr) was investigated after austempering for 1 hour at 300^{o}C. Microstructural heterogeneity was investigated at different scales using optical microscopy, scanning electron microscopy (SEM), electron probe micro analysis (EPMA), X-ray diffraction (XRD), and hardness measurements. Observed heterogeneities were related to the presence of thermal gradient, chemical segregation, and carbon gradient.

The results gave insights into the effect of the processing route on the microstructure. After austempering, bainitic ferrite, martensite-austenite islands, and carbide particles were observed. The thermal gradient was confirmed by the identification of auto-tempered M-A islands due to the slower cooling rate in the bulk of the material. Moreover, chemical segregation of Si, Mn, and Cr parallel to the rolling direction was observed and confirmed from optical microscopy, SEM, and EPMA results. In regions with high concentrations of substitutional elements, the B_s temperature was locally reduced and the bainitic ferrite formation kinetics was slow. Carbon gradient in M-A islands was observed as carbide precipitation occurred at the center of the island indicating that the carbon content was lower compared to at the edges of the constituent. Furthermore, in areas of the trailing arm with lower fractions of retained austenite ($< 8\%$), bainite formation was ceased based on the T_o curve (austenite reached a specific carbon content over which growth of bainite based on the diffusionless theory is not possible). These results indicate that bainitic ferrite advances non-uniformly through the trailing arm.

Based on these indications, the carbon gradient had a more significant effect on the bainitic ferrite formation in the spring steel during austempering compared to the thermal gradient and chemical segregation.

CONTENTS

LIST OF FIGURES

LIST OF TABLES

List of Abbreviations

AHSS	Advanced High Strength Steels
CP	Complex Phase
TRIP	Transformation-induced Plasticity
DP	Dual Phase
TWIP	Twin-induced plasticity
Q&P	Quenching and Partitioning
CFB	Carbide-free bainite
B_s	Bainitic start temperature
M_s	Martensitic start temperature
Q & T	Quenching and Tempering
ADI	Austempered Ductile Cast Iron
RT	Room Temperature
RA	Retained Austenite
M-A islands	Martenisite- Austenite islands
PAGB	Prior Austenite Grain Boundaries
PAGS	Prior Austenite Grain Size
BF	Bainitic Ferrite
CCT curve	Continuous cooling transformation curve
ND	Normal Direction
TD	Transverse Direction
RD	Rolling Direction
SEM	Scanning Electron Microscopy
EPMA	Electron Probe Micro Analysis
XRD	X-ray Diffraction
TTT curve	Time-Temperature-Transformation curve
HCSER	High content of substitutional elements region
LCSER	Low content of substitutional elements region

C.R.	Cooling Rate
EBSD	Electron Backscatter Diffraction
TEM	Transmission Electron Microscopy

1

INTRODUCTION

1.1. ADVANCED HIGH-STRENGTH STEELS

One of the major aims of the automotive industry is to achieve low fuel consumption together with high passenger safety. For these reasons, advanced high-strength steels (AHSS) have been developed over the last decades as ideal candidates for this application due to thin sheet production, high formability, and lightness [1].
Figure 1.1 illustrates the final elongation and tensile strength of the AHSS together with some conventional high-strength steels. Three generations of AHSS have been developed so far[2]:

- The **first generation** of AHSS shows a better combination of strength and ductility than conventional steels. Such materials were complex phase (CP) steels, transformation-induced plasticity steels (TRIP steels), and dual phase (DP) steels.
- In the **second generation** of AHSS, steels were included with the final microstructure containing a specific fraction of retained austenite (0.10-0.20) to enhance ductility. To achieve austenite thermal stability, alloying elements such as Mn and Ni are added which increases the production cost. Some examples are twin-induced plasticity (TWIP) steels and austenitic stainless steels.
- The **third generation** is based on the development of steels with high strength and ductility but low cost by introducing new process methods such as austempering and adding smaller amounts of alloying elements. Thus, quenching and partitioning (Q&P), carbide-free bainitic (CFB), and medium Mn steels were developed [3].

1.2. AIR SUSPENSION SYSTEMS

Air suspension system technologies have been developed over the years in the automotive industry to reduce vibration during the motion of the vehicle.

1

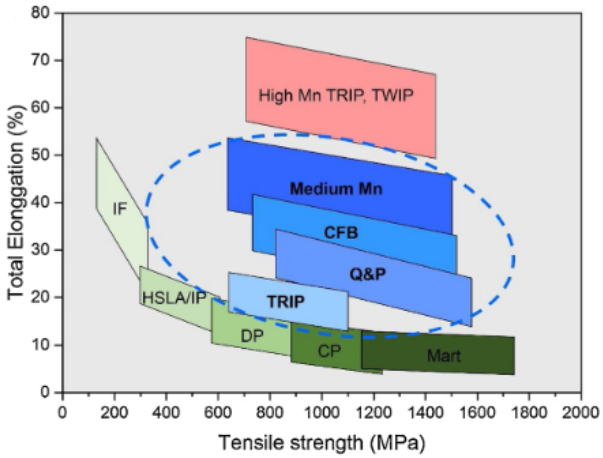

Figure 1.1: Classification of steel families according to their combination of total elongation (%) and tensile strength (MPa), CFB= Carbide free bainitic, TRIP= Transformation induced plasticity, DP = Dual Phase, Q&P= Quenching and partitioning, IF= Interstitial Free, TWIP= Twinning Induced Plasticity, HSLA= High strength low alloy [3].

In figure 1.2, an air suspension system for trucks is illustrated. One of the main parts of the system is called **trailing arm** (indicated with an arrow) and is made of steel. These steels are usually referred to as **spring steels** as they meet the required mechanical properties for this application: fatigue strength, and corrosion resistance [4]. In heavy vehicles, spring steels are AHSS as they are multi-phase materials that could meet the requirements mentioned above.

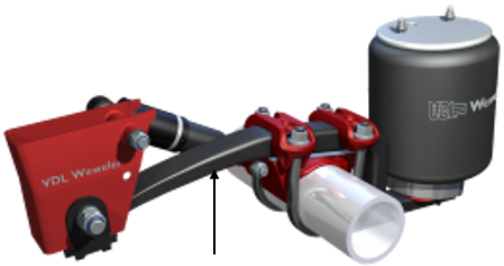

Figure 1.2: Air suspension system for heavy vehicles [5].

Many studies have been conducted to improve spring steel's performance in terms of fatigue properties by adding alloying elements like silicon, manganese, and chromium

or by applying different heat treatment processes such as quenching and tempering or austempering leading to different microstructures. In the last years, the presence of bainite in AHSS has grown great interest due to martensite's lack of ductility and the possibility of increased performance through the TRIP effect. Bainite is then formed through the application of an isothermal heat treatment named austempering. However, this microstructure production presents challenges in large-scale applications due to bainite's complex mechanisms of nucleation and growth that will be analysed in the literature review.

1.3. AIM AND STRUCTURE OF THE THESIS

This thesis aims to provide insights into the microstructural distribution of silicon spring steel after austempering.

This thesis is divided into six main chapters.

- In **Chapter 2**, a literature review is provided on silicon-containing spring steels and heat treatments. Based on this information, three reasons are indicated for the investigation of microstructural distribution.
- **Chapter 3** consists of the analysis of the spring steel used in this investigation, and the description of the experimental procedures conducted in this study.
- In **Chapter 4**, the results obtained from the experimental investigations are presented.
- In **Chapter 5**, results are discussed with respect to the research questions and research from the literature.
- The conclusions and recommendations for future work are presented in **Chapter 6**.

2

LITERATURE REVIEW

2.1. MOTIVATION

Spring steels used in air suspension systems, have developed a plurality of mechanical properties such as good fatigue resistance as well as high elastic and yield strength due to spring's high-frequency dynamic load work and need for long endurance life [6]. These mechanical properties are significantly affected by the microstructure of the steel.

The use of spring steels containing over $1.5 wt.\%$ silicon in such applications has increased over the years. This fact is attributed to the production of a carbide-free bainitic (CFB) microstructure. Generally, austempering (isothermal transformation in the bainitic range) is one of the processing methods implemented at spring steels that could lead to a CFB microstructure with stabilized austenite at room temperature. However, experiments conducted on this type of steel, lead to the conclusion that microstructural inhomogeneity was formed which influences accordingly material's mechanical properties.

The explanation of microstructural inhomogeneity requires a deep understanding of the following components. Firstly, the specific type of material needs to be understood, and more specifically, the effect of chemical composition on the microstructure. These aspects will help to comprehend the relationship between microstructure and the desired mechanical properties for the optimal spring performance. Moreover, microstructural development during austempering should be reviewed for the study of inhomogeneity. Furthermore, the application of austempering in silicon spring steel, the effect of different process parameters such as treatment temperature and holding time on the microstructure, and the response of the steel to the applied loading are analysed. Finally, a scientific basis is created on which the reasons that lead to possible microstructural inhomogeneity of this type of steel are built.

Figure 2.1: Trailing arm for air suspension system made from silicon spring steel [5].

2.2. SILICON-CONTAINING SPRING STEEL

The materials used for springs are separated into metals and nonmetallic. Such metals are steel, nickel alloy, and others. These materials are heat-treated during the spring manufacturing process to obtain the desirable properties (tensile strength, hardness) or acquire the required mechanical properties before the spring forming. Several steels could be used for this application depending on their chemical composition and heat treatment. Some of them that are used for hot forming are: Si, Mn, Si-Cr, Cr-Mo, Si-Ni-Cr, Si-Cr-V, and Ni-Cr-Mo and any standards are used to express spring steel and their chemical composition like JIS, SUP, ISO or AISI [7].

In figure 2.1, a trailing arm (leaf spring) made from silicon spring steel that is used in an air suspension system is presented [5].

Understanding the effect of chemical composition and how the microstructure of silicon spring steels develops during austempering, are factors that will contribute to the comprehension of inhomogeneity's formation. In the following sections, the effect of the spring's alloy elements and process parameters on the microstructure, and the effect on the mechanical performance, are analysed.

2.2.1. ALLOYING ELEMENTS

Silicon is the major alloying element of silicon spring steels and is added also over $1.5 wt.\%$, to improve the strength of the matrix while remaining in solid solution, which increases the material's sag resistance. Its addition is essential for steel to acquire an ausferritic microstructure during austempering. More specifically, it delays the precipitation of cementite. Generally, the presence of cementite causes fracture in high strength steels and makes the material susceptible to void formation [8]. Furthermore, silicon is responsible for the formation of surface defects and decarburization and its volume fraction in steel should be controlled [9].

Other alloy elements that influence the final microstructure of silicon spring steels are carbon, manganese, chromium, and vanadium.

Carbon presents a strong influence on the bainite-start temperature (B_s) as it decreases with a rise in carbon content. Carbon has higher solubility in austenite than in ferrite. Thus, high carbon content stabilizes austenite, leads to lower bainitic transformation temperatures, and retards the incubation period of bainite reaction [10] [11]. Also, the maximum attainable volume fraction of bainitic ferrite decreases. Besides B_s, martensitic start temperature (M_s) is decreased by the increasing carbon content. There is a wide range of carbon addition to spring steels from 0.40-0.65 $wt.\%$ [12].

Manganese and chromium are added to increase the silicon spring steel's hardenability. Manganese is usually between 0.5-1.1 $wt.\%$ in silicon spring steels [12]. Chromium is also a strong carbide former which in high silicon steels tends to prevent decarburization [7] and is added from 0.2-1.2 $wt.\%$[12]. However, both Mn and Cr tend to segregate and form bands which can cause retardation of bainite kinetics in regions rich in these elements. It was proven also, that at high isothermal treatment temperatures (close to B_s), Cr retards the interface mobility, and thus, bainitic ferrite growth is also, delayed [9].

Vanadium is frequently added to this type of steel (0.1-0.2$wt.\%$) to form carbides that lead to an increase in hardness. Moreover, vanadium carbides are stable even at high temperatures and thus, contribute to the restriction of austenite grain growth during austenitization [9].

2.2.2. QUENCHING & TEMPERING (Q & T) PROCESS

Usually, the processing of spring steel involves casting and rolling to obtain the shape of the trailing arm. However, the last years forging has been applied instead of rolling in favor of acquiring a finer microstructure [13]. After rolling or forging, different heat treatment routes can be designed to obtain the required properties. One of these heat treatments is the quenching & tempering (Q & T) process. Typical Q & T includes austenitization, quenching of austenite to room temperature to form a fully martensitic microstructure, and a heat-treatment at temperatures above M_s to obtain tempered martensite. Figure 2.2 illustrates this heat treatment including forging, austenitization and quenching & tempering.

Even when Q & T results in the strength increase of spring steel, this route could lead to quench cracking or the production of undesirable residual stresses affecting spring performance negatively [15].

Routes alternative to the typical Q & T are being investigated to produce components with equivalent properties while reducing energy consumption. One of the main alternatives is austempering, which leads to a bainitic microstructure. Austempered commercial spring steels with bainitic microstructure present improved mechanical properties such as tensile strength compared to Q & T processed spring steel [16].

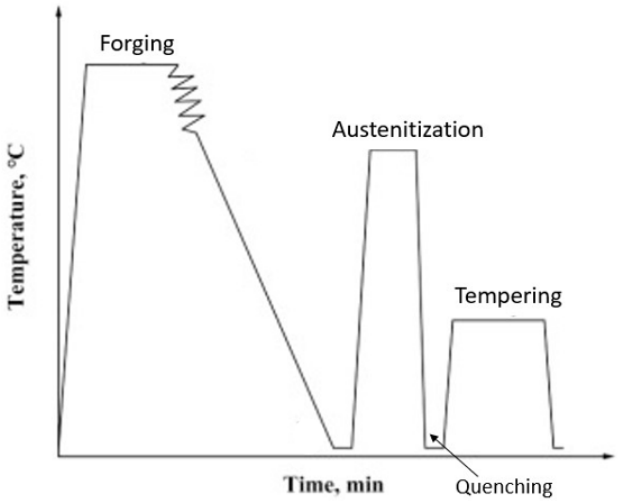

Figure 2.2: Schematic overview of Quenching and Tempering applied at silicon spring steel [14].

2.2.3. AUSTEMPERING HEAT TREATMENT

Austempering is an isothermal heat treatment that is applied to ferrous alloys such as steel and cast irons. The main aim of this process is to obtain a microstructure that consists of ferrite and carbon-rich austenite (ausferritic structure) for cast iron and bainite for steel. The austempering process route for steel is illustrated in figure 2.3 where the material is quenched from austenitizing temperature fast enough to avoid the formation of pearlite and is held isothermally at a temperature above M_s to avoid martensite formation [17]. After the isothermal treatment, the material is cooled to room temperature. Due to the outstanding combination of properties such as strength and ductility, the process is used in many industries like automotive.

Bainite's formation mechanism and kinetics in steels present great complexity [18]. Understanding this transformation together with its diversity in morphology and influence of chemical composition, are considered essential factors for the later comprehension and explanation of the spring steel's microstructure variations.

2.2.3.1. BAINITE FORMATION

When the material is held at temperatures below pearlite formation, austenite decomposition occurs leading to a microstructure consisting of plate-shaped ferrite and carbides named **bainite**. The bainite formation has grown great controversy over the years about whether it forms via a **displacive** or **diffusion-controlled** mechanism. In the literature, both theories are supported.

The **diffusionless theory** considers that the bainite transformation has many similarities with martensite transformation[3]. Bhadeshia introduced that ferrite in bainite forms via nucleation and diffusionless growth and the following conditions must be ful-

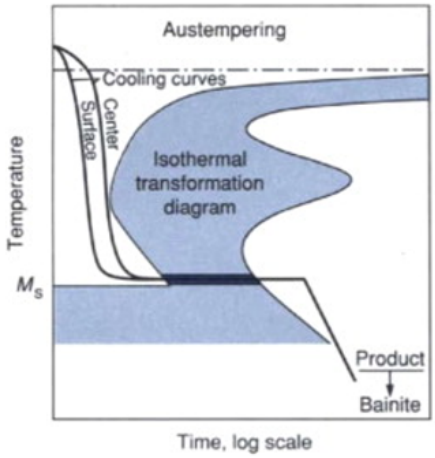

Figure 2.3: Austempering treatment for steel with the final product being bainite [19].

filled: the driving force for the transformation of austenite to ferrite must exceed the energy barrier for bainite formation (400 $Jmol^{-1}$) and the maximum driving force for nucleation must be higher than the value given by the general nucleation function[20] [21].

In figure 2.4, bainite nucleation and growth during austempering according to the **displacive theory** are schematically shown. The diffusionless theory states that ferrite plates start to nucleate at austenite grain boundaries (stage I) and grow in clusters called sheaves [10]. The plates inside each sheave are called sub-units and have a common crystallographic orientation. This bainite formation, at the initial stages of transformation, leads to an increase in the number density of nucleation sites [22]. Since this nucleation occurs at the austenite/austenite interface, the prior austenite grain size (PAGS) affects the morphology and kinetics of bainite. As bainitic ferrite generates, it nucleates at the bainitic ferrite/austenite interfaces (stage II). This nucleation is called autocatalytic [23][24].

At stage III, the austenite/austenite interfaces are a minority compared to austenite/ bainitic ferrite and available interfaces of austenite for nucleation start to decrease. Thus, bainite nucleates at a lower rate at the austenite/ferrite interface, and the sheaf structure develops as this process continues. Furthermore, bainitic sheaves thicken during this stage. Bainite, in general, seems to grow at small driving forces compared to martensite formation due to higher transformation temperatures involved [10].

From the remaining austenite which is rich in carbon, carbides start to precipitate between each plate in a sheaf (sub-units). Thus, bainite forms at two separate stages: the formation of ferrite and the precipitation of carbides. The most common carbide that forms is cementite but other carbides were also detected such as transition carbides

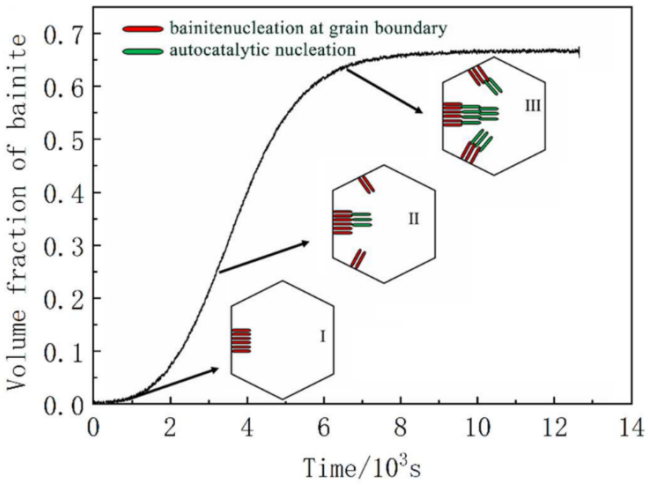

Figure 2.4: Bainite nucleation and growth during austempering in a high Si, medium C steel [23].

in high silicon steels [20]. The formation of carbides depends on the transformation temperature applied and the chemical composition of the material [25]. As the growth of bainite occurs, the Gibbs-free energy of austenite starts to decline as carbon starts to partition from bainitic ferrite to austenite, and at some point, it obtains the same value as that of ferrite at the same chemical composition, as presented in figure 2.5. The temperature at which the free energy of austenite is identical to that of ferrite is called T_o temperature. Ferrite is allowed to form without diffusion, as long as the carbon concentration in the austenite is below the T_o-line [26]. In figure 2.5, the T_o-curve is illustrated with the T_o'-curve that was introduced by Bhadeshia, where the energy barrier for the growth of bainitic ferrite (which was related to the transformation strain) was considered.

Bainite formation shows an 'incomplete reaction phenomenon' where the carbon concentration of the untransformed austenite on the cessation of bainite transformation remains below the level determined by the para-equilibrium condition [27]. In other words, diffusionless transformation becomes thermodynamically impossible as the free energy of bainitic ferrite is higher than the one of austenite [28].

Different models are available in the literature for describing the **diffusional** growth of bainitic ferrite. For example, Hillert, Höglund, and Ågren proposed that the growth mechanism of bainitic ferrite is similar to the Widmanstättern ferrite's and the growth rate is controlled by the diffusion of carbon in austenite (WBs theory). Furthermore, Aaronson, Reynolds, and Purdy suggested the solute drag theory and the bainitic ferrite formation results from eutectoid decomposition like pro-eutectoid ferrite [30].

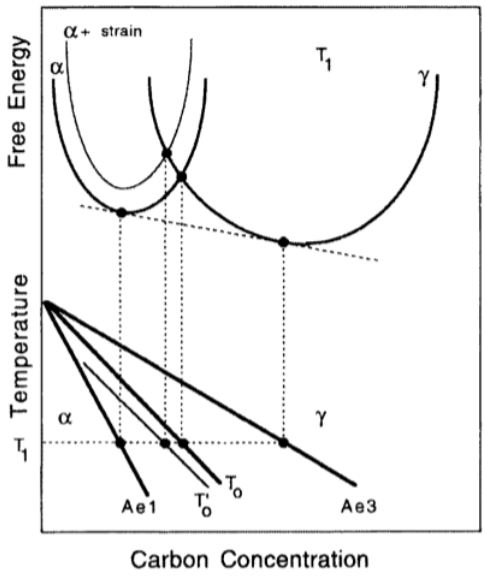

Figure 2.5: Schematic illustration of T_o and T_o'-curve and the Gibbs free energy curves of ferrite and austenite below A_1 temperature [10] [26].

The formation of bainite depends on temperature, the chemical composition of steel, and holding time. The temperature B_s is defined as the temperature above which no bainite forms and it variates mostly according to the chemical composition of the steel. The transformation temperature affects, for example, the morphology of bainite.

According to the morphology, bainite could be distinguished into (a) upper and (b) lower bainite. Figure 2.6 illustrates differences between the two bainite morphologies and formation mechanisms. The temperature transformation is higher in upper bainite than in lower bainite where carbides precipitate both from the C-rich austenite and supersaturated ferrite. While upper bainitic ferrite is free of carbides, in lower bainite diffusion is slower and carbides precipitate at supersaturated ferrite[20].

2.2.3.2. CARBIDE-FREE BAINITIC (CFB) STEELS

Before steel, another material that has been processed with austempering was austempered ductile cast iron (ADI) which has grown great interest due to the outstanding combination of excellent properties such as high strength, great ductility, and good fatigue properties. This could be attributed to the bainitic microstructure.

In recent years, studies have been focused on applying the same process of austempering to steel, acquiring an ausferritic microstructure, and overcoming the limitations of ADI.

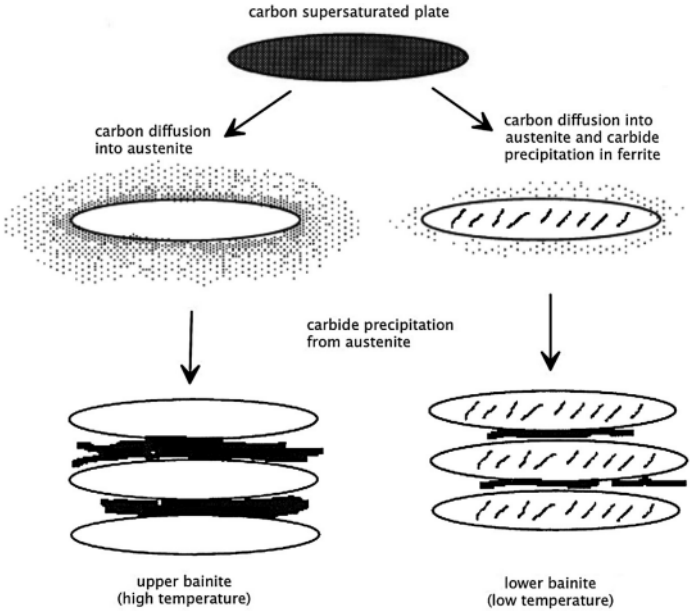

Figure 2.6: Illustration of transition from upper to lower bainite [10].

To achieve an ausferritic microstructure, there are two important aspects to consider austempered steels usually contain a significant amount of Si (over $1.5 wt.\%$) and thus, no precipitation of cementite occurs [31] [32] [33]. Cementite formation, not only is a possible fracture initiation site but also, reduces the amount of carbon available to enrich austenite. If the carbon content of austenite is low when the temperature reaches the T_o curve during cooling at room temperature (RT), austenite will transform to martensite due to its low stability. By adding substitutional solutes that could shift the T_o curve to greater carbon concentrations and by applying low transformation temperature, the carbon content of austenite will increase which will lead to an increase in the fraction of bainite and a decrease in martensite formation [34].

The nucleation and growth of bainite during austempering in spring steel occurs as described in section 2.2.3.1. Carbon has low solubility in bainitic ferrite and thus, the excess of carbon diffuses from bainitic ferrite's sub-units and is available to enrich austenite [35]. Based on the **diffusional theory**, bainite ferrite could grow also by inheriting the carbon content of the parent austenite [9]. In any case, the final microstructure after isothermal heat treatment includes bainitic ferrite and retained austenite enriched with carbon.

Retained austenite (RA) at RT favors the transformation-induced plasticity (TRIP)

effect as when mechanical loading is applied to the austenite phase, it might be transformed to martensite. As a result, the material's properties such as strength and ductility would improve [25] [36] [37]. These types of steels that contain a significant amount of silicon in which cementite formation is suppressed are called carbide-free bainitic (CFB) steels or ausferritic steels. For these reasons, CFB steels present a good combination of strength and ductility and they are used in many applications such as springs, rails, and bearings.

2.2.3.3. EFFECT OF PROCESS PARAMETERS ON THE MICROSTRUCTURE

Similar to other processes, austempering parameters such as temperature and time influence greatly the thermodynamics and kinetics of bainite transformation and the diffusion process of carbon during the transformation. Hence spring steel microstructure and properties are affected.

High temperatures (over 400^oC) and long holding times (2 h) applied at spring steels lead to the formation of lath bainitic ferrite and the precipitation of carbides, despite steel's significant amount of silicon [38]. The carbide formation can be attributed to the long holding time (2 h) as they have time to start precipitating [39] [40]. Furthermore, it has been proven that carbon may remain in solid solution in bainitic ferrite and not enrich the retained austenite [41].

The effect of holding time on the microstructure is indicated in figure 2.7 where the fraction of retained austenite is plotted against holding time for silicon steel ($1.7 wt.\%$) with akin chemical composition to spring steel at different temperatures [38]. With the increase of holding time (10-60 minutes), the fraction of RA decreases as the bainitic ferrite transformation progresses and carbides start to precipitate. Lower treatment temperatures affect the stability of austenite, as time for carbon partitioning is restricted. This occurs as at low temperatures, the driving force for austenite to bainitic transformation is higher [38]. As a result, the carbon enrichment of austenite is sluggish and austenite is not stable and its amount decreased as treatment temperature declined [17].

The work of Timokhina et al. on a steel with a very similar chemical composition ($1.6 wt.\%$ Si) to silicon spring steel shows that after austenitization and isothermal heat treatment, apart from bainitic ferrite[41], two different morphologies of retained austenite can be also, observed: **film-like** and **blocky**. Similar findings were confirmed by other studies focusing on high silicon steels with medium carbon content ($0.5-0.6 wt.\%$ C)[23][42]. Figure 2.8 presents these two morphologies in a medium carbon high silicon steel after applying austempering at 330^oC and 300^oC for 4 and 8 hours respectively. Blocky austenite is usually located between bainite sheaves while films of austenite are observed between sub-units [43]. It is clear from figure 2.8 that films of austenite and bainitic ferrite are finer when the austempering temperature is lower [23]. Blocky austenite at RT was found also, to contain less carbon compared to filmy austenite and is also referred to as martensite-austenite (M-A) islands since unstable austenite transforms to martensite during cooling at RT [44] [45].

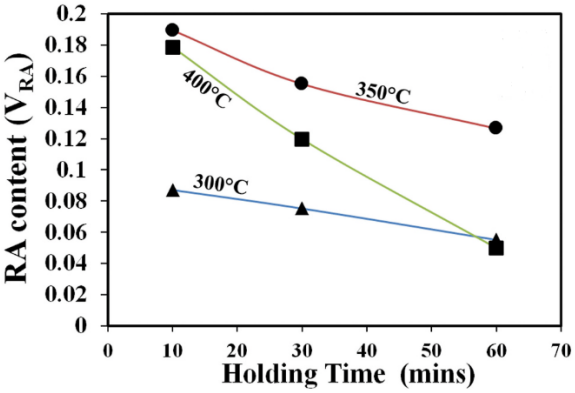

Figure 2.7: Variation in the fraction of retained austenite (V_{RA}) withholding duration during austempering at different temperatures in a high silicon steel [38].

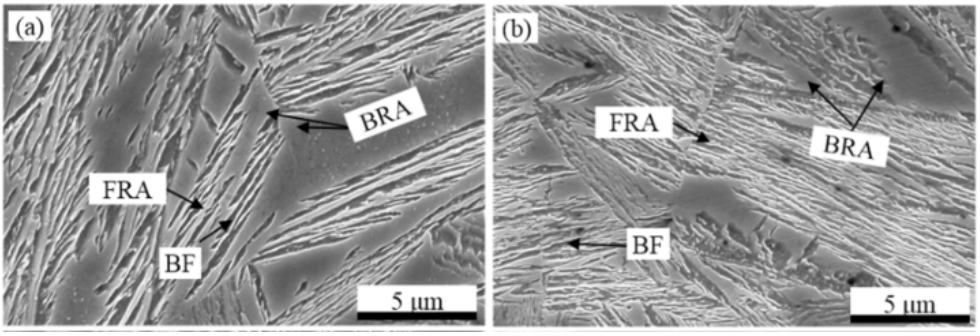

Figure 2.8: Microstructure of a medium carbon high silicon steel after applying austempering at (a) 330^{o}C and (b) 300^{o}C. FRA is film retained austenite, BRA is blocky retained austenite, and BF is bainitic ferrite [23].

M-A islands are observed mostly along the prior austenite grain boundaries (PAGB). Carbon concentration at the center of M-A islands was found to be low compared to the enriched edges [46]. Figure 2.9 shows the microstructure of a CFB steel after an isothermal heat treatment at 400^{o}C for 15 minutes where M-A islands were identified.

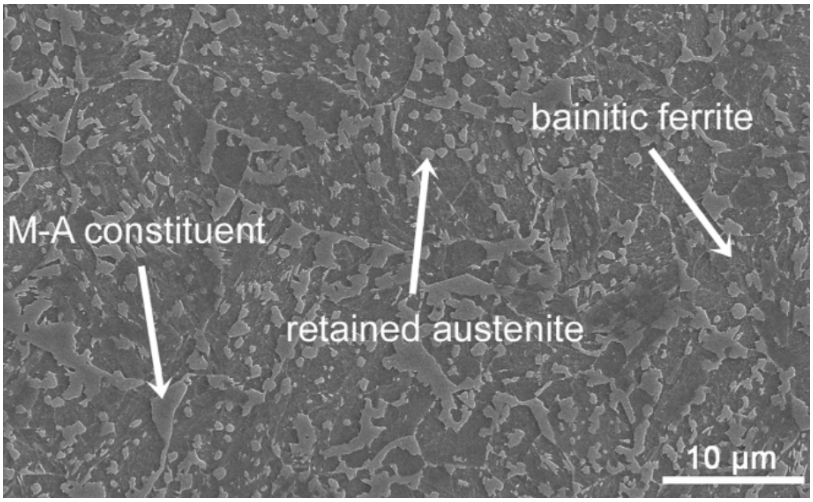

Figure 2.9: SEM micrograph of a CFB silicon steel after isothermal treatment at 400^{o}C for 1000 s. [35].

Prior austenite grain size (PAGS) was found to influence the morphology and thickness of carbide-free bainite in austempered steel with similar chemical composition to silicon spring steel except for a carbon content of 0.25 % wt that usually in spring steel is higher[47]. However, the dimensions of M-A islands were higher in coarse grains [42]. In finer PAGS (20 ± 6 μm), the grain boundary area per unit volume of austenite increases leading to the formation of finer bainitic ferrite sheaves [47]. In addition, the incubation period for bainite's formation was shortened in finer PAGS [48]. Thus, wide distribution in the grain size of the material, caused by heat treatment, could explain possible differences in the microstructure.

To summarise this section considering austempering applied to silicon spring steel, the stabilization of retained austenite at room temperature is one of the main goals of this process. Carbon distribution across the material plays a significant role in the amount of austenite that will be retained, together with the addition of silicon and manganese that contribute to the stabilization of austenite. The process temperature and time influence significantly the CFB microstructure in terms of phases, morphology, and thickness. All these factors were reviewed to detect possible microstructural inhomogeneity.

2.2.4. MECHANICAL PROPERTIES

According to Kim et al., austempered spring steel presented higher tensile strength (1880 MPa) than Q & T spring steel (less than 1800 MPa) [17]. However, CFB steels with comparable chemical composition to silicon spring steels that contained large M-A islands in the structure after austempering, presented low tensile strength and impact toughness as they acted as damaging sites. Specimens with a lower amount of martensite at RT exhibited improved tensile properties and work hardening behavior due to the TRIP ef-

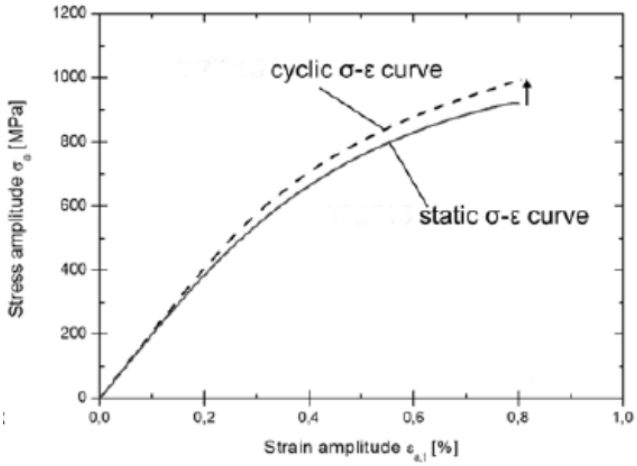

Figure 2.10: Cyclic stress-strain curve of carbide-free bainitic steel after isothermal heat treatment [49].

fect. The presence of carbon enriched austenite at room temperature presents low stress concentration, and thus, crack initiation and propagation could be precluded [46].

In figure 2.10, the cyclic stress-strain curve of a carbide-free bainitic forged steel with akin chemical composition to spring steel obtained by Wirtus et al. is shown [49]. The steel presented cyclic hardening due to the TRIP effect as the static stress-strain curve (obtained by tensile testing) is located lower than the cyclic (obtained by incremental step tests)[49]. This hardening could be attributed to the presence of film austenite which favors the TRIP effect under fatigue cyclic loading, contributing to the improvement of fatigue performance [50]. Moreover, cracks were found to propagate steel when blocky austenite (M-A islands) was present [51].

Apart from austenite, the thickness of bainitic ferrite plays an important role in fatigue strength as thicker laths provide a smaller mean free path for dislocation glide increasing the strength of the material [52]. Silicon spring steel austempered at low temperatures (275^{o}C) presented also, higher fatigue strength after high cycle fatigue testing (950 MPa) than at higher temperatures (at 300^{o}C it was 850 MPa) [50]. Fatigue strength is one of the most important properties of spring steel which ensures long-term reliability.

It is clear that when steel presents microstructural variations, mechanical properties such as tensile and fatigue strength will also display inhomogeneity accordingly. In the next section, factors that influence the carbon content of austenite and bainitic ferrite's volume fraction and thickness which could also explain differences in microstructure will be analysed.

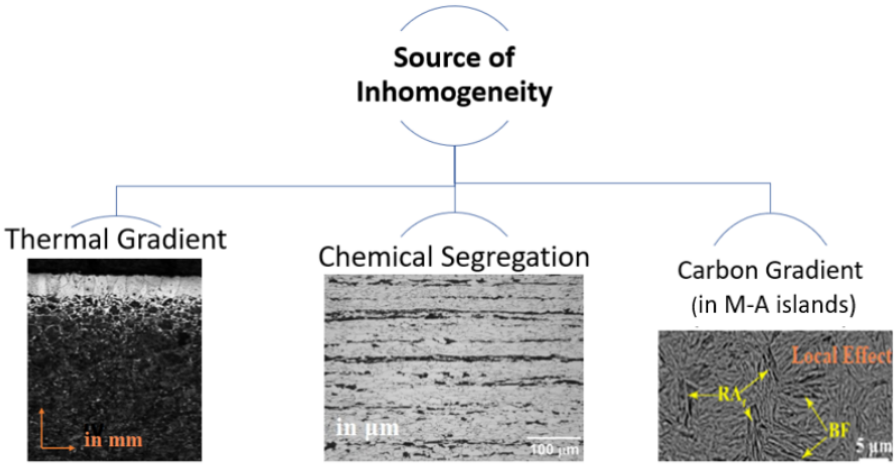

Figure 2.11: Possible reasons explaining microstructural inhomogeneity in silicon spring steel, RA= Retained Austenite, BF=Bainitic Ferrite [46] [53].

2.3. POSSIBLE SOURCES OF INHOMOGENEITY IN SILICON SPRING STEELS

Explaining possible reasons that prompt microstructural inhomogeneity and recommending possible solutions are essential to improve the spring's performance. Possible sources of inhomogeneity are: thermal gradient through-thickness of the material, chemical segregation from solidification, and local carbon gradient. In figure 2.11, sources of inhomogeneity mentioned are summarized with an indication of the length scale of observation. In the following, inhomogeneity will be examined from different perspectives reaching valuable conclusions.

2.3.1. THERMAL GRADIENT

During heat treatment, temperature distribution through thickness of the material during heating and cooling could lead to the formation of different microstructures. Before austempering, steel cools down from austenitization, and after austempering, it cools down at RT. Figure 2.3 indicates the cooling curves during austempering treatment for steel. Bulk has a slower cooling rate compared to the surface of the material. This means that the isothermal temperature is reached at a later stage in the bulk than on the surface of the material.

Figures 2.12 and 2.13 present the temperature distribution of a low silicon ($0.4 wt.\%$) leaf spring steel after austenitization and right after oil quenching for 10 minutes, respectively. Temperature ranges from 750^oC to 890^oC in figure 2.12 and from 74^oC to 140^oC in figure 2.13 based on the thickness of the spring. In zone 1 where the thickness of steel is lower (14 mm), the temperature distribution was more homogeneously distributed than in zone 2 where the thickness is higher (40 mm). According to figure 2.12,

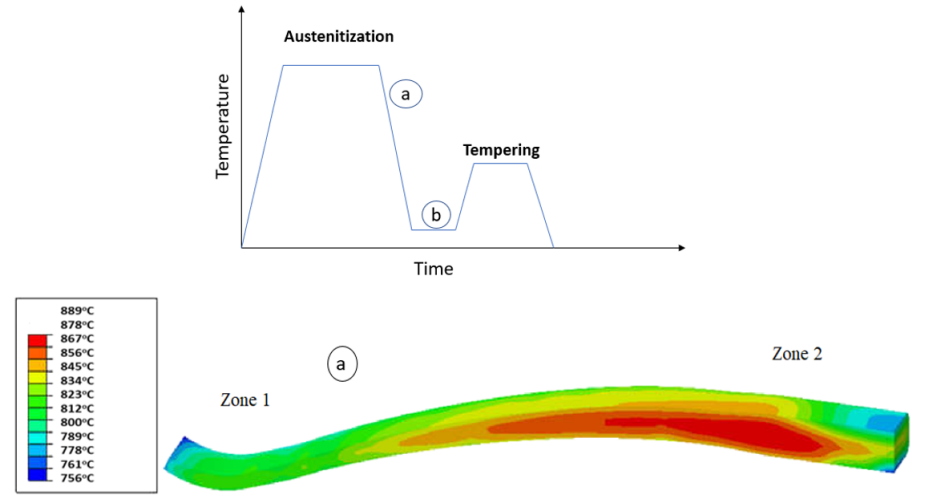

Figure 2.12: Temperature distribution of low silicon spring steel (51CrV4) after austenitization and before quenching [54].

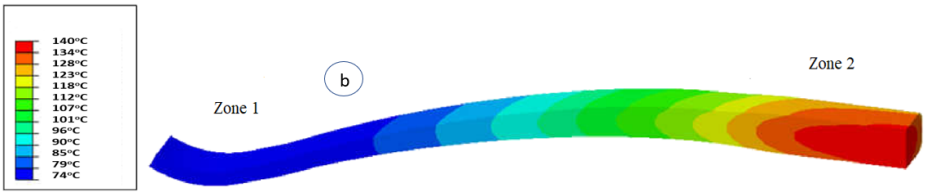

Figure 2.13: Temperature distribution of low silicon spring steel (51CrV4) after oil quenching[54].

temperature variations between the surface and the bulk of the material were developed during cooling. In figure 2.13, the two zones demonstrated significant variations in temperature [54].

These results indicate that during heat treatment (austenitization, austempering), the temperature may be different through the material and the cooling rate may variate accordingly across the thick parts of the spring leading to the formation of different microstructures at the surface with respect to the bulk.

Studies focused on the influence of different cooling rates on the carbide-free bainitic microstructure of silicon steel and proved that when slow cooling was applied (0.1 K/s, 0.5 K/s) after austempering, bainite sheaves had more time to nucleate and grow [24]. Bainitic ferrite during fast cooling (3 K/s) was finer and the bainitic transformation was suppressed. As a result, there was not enough time for carbon to enrich austenite, leading to the formation of martensite. After slow cooling, specimens presented ϵ carbides

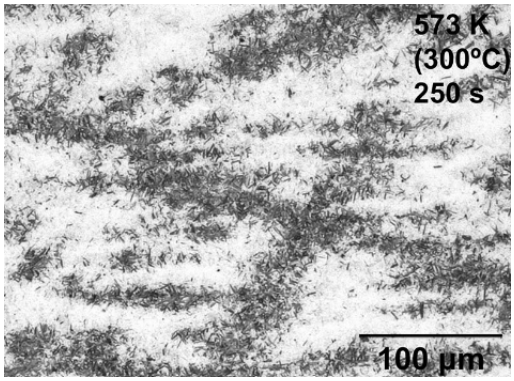

Figure 2.14: Banded microstructure of medium carbon low silicon spring steel after austempering at $300^{o}C$ for 250 s [9].

precipitated in bainitic ferrite laths [24].

Ackermann et al. investigated the effect of cooling variations on the microstructural heterogeneity of bainitic steel containing 1.2 % Si [55]. When the cooling rate crossed the upper bainite region in the continuous cooling temperature (CCT) diagram (2 K/s and then, 1 K/s), the microstructure was inhomogeneous. Grain coarsening in the upper bainite region and different morphologies in length and shape of bainitic ferrite, complicated carbon partitioning to austenite [55].

Based on the literature, in regions where the material is fast cooled, M-A islands are expected to be present due to the instability of austenite. However, in the bulk of the material, a higher amount of bainitic ferrite and possible carbide precipitation will be probably formed affecting the final ausferritic microstructure. This microstructural variation is forecasted to be observed in parts of the spring with higher thicknesses.

2.3.2. CHEMICAL SEGREGATION

The basic alloying elements of silicon spring steels are manganese and chromium which tend to segregate during solidification. Goulas et al. found differences in the bainite formation kinetics in a low silicon spring steel, due to local inhomogeneity in Cr and Mn concentration and formation of bands, resulting in retardation of the growth and volume fraction of bainite in the high Mn and Cr concentration regions [9]. This occurs because Mn and Cr reduce the driving force for ferrite formation. Figure 2.14 illustrates the banded structure that occurs due to the chemical segregation of Mn and Cr. It is clear that the bainitic ferrite's (dark-etching phase) nucleation is not homogeneous and the white etching phase was considered martensite or austenite.

After casting and forging, different prior austenite grains sizes may form in a subsequent austenitization. Basso et al. presented the PAGBS distribution after applying austempering at high silicon (2.2 %) high carbon cast steel [56]. Close to inclusions and

micro-shrinkage regions, grains were finer. This fact was attributed to the possible segregation of Si, Mn, and Cr where the last austenite grains tend to form [56] [57]. In these grains, bainite reaction kinetics will be slower leading to different final phases and morphologies through steel.

These elements also decrease the activity of carbon and tend to attract it to Mn- and Cr-rich regions. Consequently, carbon segregation in the same regions as segregation of substitutional alloy elements could influence the stability of austenite. This occurs because the available carbon content to partition to austenite will decrease. Carbon segregation was identified in dislocations in bainitic ferrite by Caballero [58] and Goulas et al.[9]. Regions rich in carbon could indicate the onset of the transition carbides observed during tempering [59].

Consequently, chemical segregation limits both the final bainite fraction and stability of austenite proving that alloy element segregation spring steel influence undoubtedly the final microstructure distribution.

2.3.3. CARBON GRADIENT

A silicon spring steel could contain carbon gradient in the retained austenite islands due to bainite's formation. If short austempering time is applied, the C concentration at the interface of austenite/bainitic ferrite may reach the value defined by the T_o curve and the formation of bainitic ferrite may be hindered if it is considered that it forms based on the diffusionless theory[60]. Carbon diffusion at the center of the blocks will be then, limited and austenite will be enriched with carbon only at the interface. Thus, coarse M-A islands may be present at RT with martensite formed at the center of the island.

Carbon gradient can be further affected by the presence of thermal gradient and chemical segregation.

2.4. SUMMARY

The process of austempering and the effect of chemical composition, temperature treatment, and time on the microstructure and mechanical properties of silicon spring steels, were reviewed. The main conclusions are listed below based on which inhomogeneity will be explained.

- Austempering is applied at silicon spring steels to obtain a carbide-free bainitic microstructure (ausferritic structure).
- At low austempering temperatures and short holding times lead to less retained austenite as time for carbon partitioning, was restricted. After a long holding time, precipitation of carbides occurred, affecting ausferritic microstructure.
- Thickness of bainitic ferrite and fraction of RA influences fatigue strength. Thickness is mainly controlled by the austempering temperature and finer sub-unit present higher fatigue strength. Film-like RA at room temperature inhibits crack propagation.

- Three sources of inhomogeneity were identified: thermal gradient, chemical segregation of substitutional elements, and carbon gradient which may lead to different morphologies and microstructures through the thickness of the material. Carbon gradient could occur as a result of these two facts or independently.
- Carbon non-uniform distribution causes differences locally in the stability of retained austenite. Austenite not enriched with carbon will transform to martensite during cooling.

2.5. RESEARCH QUESTIONS

The **objectives** of this master thesis are to investigate the effect of the processing route of a silicon spring steel on the microstructure with special attention to the presence of inhomogeneity and possible reasons to explain it. Furthermore, the influence of the observed inhomogeneity on the failure mechanisms of the material will be discussed. The following **sub-questions** will be addressed and formulated to assist in explaining inhomogeneity from different aspects and reach to a conclusive answer.

1. How does thermal gradient affect the final microstructure after austempering?
2. How does possible chemical segregation through the material influence the microstructural inhomogeneity of silicon spring steel?
3. What is the effect of carbon gradient in the microstructural distribution of silicon spring steel?

3

MATERIAL AND METHODOLOGY

This chapter contains a detailed description and reasoning of the experimental procedure conducted in this research. The chemical composition of investigated material is presented along with an indication of the heat treatment applied by the manufacturing company VDL Weweler for the spring steel. Last but not least, the sample preparation for each experiment is explained.

3.1. INVESTIGATED SPRING STEEL AND HEAT TREATMENT

The present work focuses on the silicon spring steel 61SiCr7 which chemical composition is given in table 3.1.

Table 3.1: Chemical composition of 61SiCr7 the spring steel used in this work.

Alloy	C	Si	Mn	Cr	P	Fe
wt.%	0.60	1.63	0.97	0.48	0.025 max	Balanced

The material is hot rolled to a round bar and then, forged to the trailing arm shape. The material then is subjected to full austenitization at 900^oC followed by austempering at 300^oC.

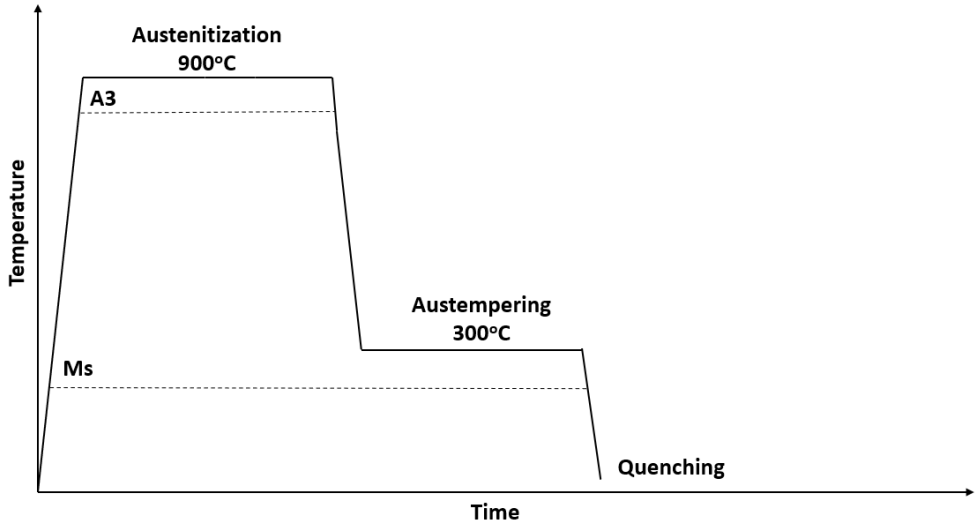

Figure 3.1: Designed heat treatment of spring steel

The austempering treatment takes place for 1 hour and afterward, the material is water quenched. Figure 3.1 presents the designed heat treatment of the spring steel. More details of the heat treatment were not provided due to being private information of the company.

Understanding microstructural development through heat treatment requires the calculation of the bainite and martensite start temperature (B_s and M_s respectively). The following equations were used for the temperatures estimation [10]:

$$B_s\,(^\circ\mathrm{C}) = 830 - 270\,w_\mathrm{C} - 90\,w_\mathrm{Mn} - 37\,w_\mathrm{Ni} - 70\,w_\mathrm{Cr} - 83\,w_\mathrm{Mo} \tag{3.1}$$

$$M_S\,(^\circ\mathrm{C}) = 539 - 423\,w_\mathrm{C} - 30.4\,w_\mathrm{Mn} - 17.7\,w_\mathrm{Ni} - 12.1\,w_\mathrm{Cr} - 7.5\,w_\mathrm{Mo} \tag{3.2}$$

where w_i represents the concentration in weight percent of the element. The temperatures reached 547^oC and 250^oC respectively. These temperatures may variate through the material based on the local chemical composition of the area.

3.2. SAMPLE PREPARATION

The trailing arm was provided by VDL Weweler and was subjected to failure testing from the company. Thus, only the head and tail parts of the arm were supplied. Samples were extracted from two different locations corresponding to two different thickness parts of the tail of the spring for investigation.

Figure 3.2 (a) indicates the head and tail of the trailing arm and the areas that were cut for further investigation. Figure 3.2 (b) presents the two parts: back and front, after final cutting which was performed using Struers Accutom-100 low-speed machine with an

aluminium oxide cut-off wheel (with 12.7 mm diameter) and rotation speed 3000 rpm. This method was opted for because it protects the material from heat deformation and provides high accuracy. For this research, it is important to use a method that would preserve the microstructure after heat treatment. Thickness in the trailing arm variates from 10 to 20 mm. The normal direction (ND), transverse direction (TD), and rolling direction (RD) were indicated in figure 3.2.

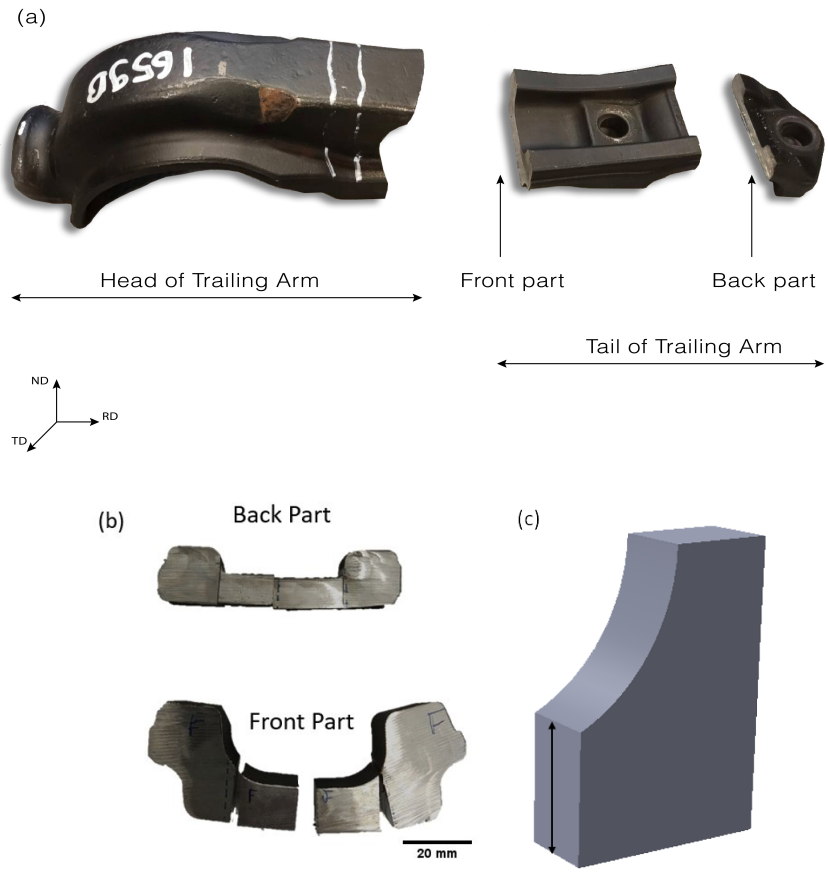

Figure 3.2: (a) Head and tail of trailing arm provided by VDL Weweler (b) Front and back part after final cutting. (c) Arrows indicate the thickness of the samples for both the front and back parts.

To investigate the different microstructures formed during austempering, a different region of each sample was selected for detailed characterization as presented in table 3.2. The first area corresponds to the normal plane of the spring steel, the second and fourth regions to transversal planes with different dimensions, and the third, to the rolling plane. This information is summarized also, in figure 3.3. Two different transversal planes were investigated to comprehend the effect of thermal gradient and chemical

segregation during heat treatment on different parts of the trailing arm. The samples are referred to based on which part they were extracted from: back (B) or front (F) part, the investigated area based on figure 3.3 and table 3.2 and which location of the area is indicated upper, middle and lower.

Table 3.2: Investigated areas of 61SiCr7 spring steel.

Number of Surface	Investigated Area
1	Normal Plane
2	Transversal plane
3	Rolling Plane
4	Transversal plane

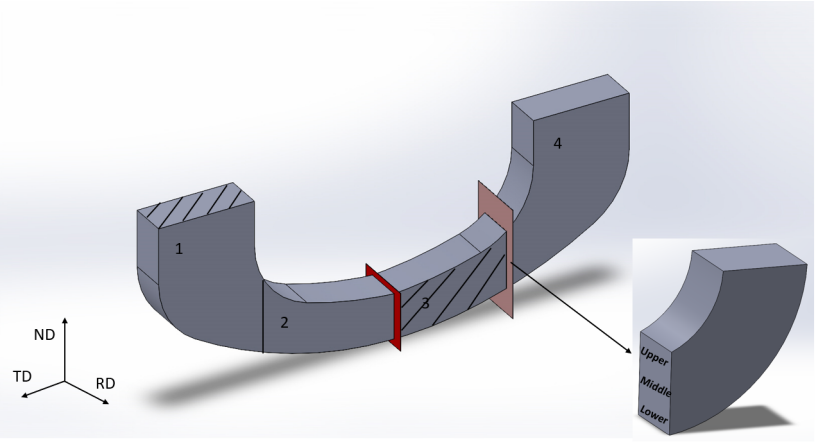

Figure 3.3: Selected regions for microstructural investigation of back (B) and front part (F) of 61SiCr7 spring steel.

The transversal plane number four has a higher thickness than that of number two. Thickness measurements were done on transverse planes indicated by arrows in figure 3.2 (c) and presented in table 3.3.

Table 3.3: Thickness of the investigated samples of 61SiCr7 spring steel measured along the normal direction.

Back Part (B)	Thickness (in mm)
2	8.50-9.30
4	11.20-12.00
Front Part (F)	**Thickness (in mm)**
2	13.10-13.90
4	16.50-17.30

3.3. OPTICAL MICROSCOPY

After final cutting, the samples were embedded using a hot mounting press machine to reduce sample damage. Figure 3.4 (a) presents the Struers LaboPress-3 mounting press machine that was used. The heating temperature was 180^{o}C and a conductive resin was used in this research. Some of the mounted specimens are shown also, in figure 3.4 (b).

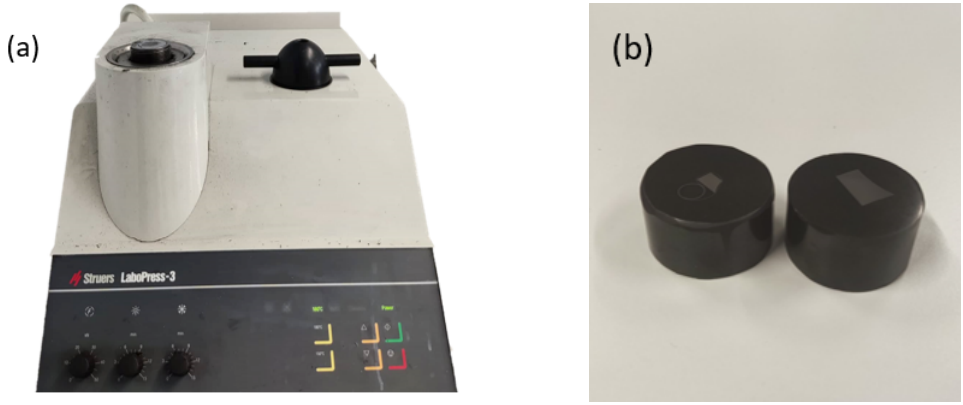

Figure 3.4: (a) Hot Mounting Press (b) Mounted Samples

Furthermore, the samples were subjected to grinding and polishing. The material was removed using silicon carbide papers with water as lubrication in a **n Struers LaboPol-25**. The process started using coarse grit silicon paper (p180 grit) and continued progressively using finer paper, finishing with p2000 grit. The next preparation step included polishing using Nap and Mol polishing cloths with 3μm and 1μm diamond liquid suspension, respectively. Both steps were done using a rotation speed of 200-300 rpm for approximately 5-10 minutes and finished when all scratches were removed.

After polishing, samples were etched using 2% and 5% Nital. The etchant's composition, which is listed to ASTM standard E407, is 1–5 mL nitric acid (HNO_3) and 100 mL ethanol (95 %) or methanol (95 %) [61]. In specimens in which etching lasted longer than 5 minutes, 5% Nital was used to accelerate the process.

Figure 3.5 illustrates the Olympus BX60M microscope where optical microscopy analysis was performed. Surfaces were observed from lower to higher magnification (from 5X to 100X). Each investigated area (see figure 3.3) was divided into sub-regions to follow the microstructure variation.

3.4. ELECTRON MICROSCOPY

3.4.1. SCANNING ELECTRON MICROSCOPY (SEM)

Scanning Electron Microscopy (SEM) was used to further analyse the phase distribution and morphology of steel in higher magnifications after optical microscopy. A JEOL JSM-

Figure 3.5: Optical Microscope Olympus BX60M used for initial analysis.

IT100 was used and images of the steel microstructure were taken with a magnification range between 1000x-10000x. The probe current applied changed from 40-60 kV based on the magnification used. For high magnifications (over 4000X), probe current of 40 kV was applied to achieve optimal resolution.

SEM was used for the quantification of M-A island size which could contribute in explaining different microstructures of spring steel. These were conducted in well etched micrographs using SEM tools and measuring the area of the grain. The area was considered cyclic (πr^2) and was calculated using image analysis software ImageJ. From the calculated area, the diameter of each constituent was measured. Based on the range of the measurements (difference between maximum and minimum value), six intervals were created. The probability was calculated by dividing the number of M-A islands (0.5-6 μm) in each interval with the total number of M-A islands calculated in each investigated surface (75 approximately per area). The standard deviation of M-A islands size and then, it was added to the M-A size measurements.

Similar procedure was followed for the quantification of PAGB size in the same samples for the M-A island size measurements. In this case, 100-120 PAGS were measured per investigated area.

Specimens were prepared in the same way as for optical microscopy. That includes grinding, polishing and etching. The same sub-regions were analyzed as in optical microscopy to be able to combine both microscopy results.

3.4.2. ELECTRON PROBE MICROANALYSIS (EPMA)

For alloying elemental distribution, a qualitative and quantitative analysis was performed using electron probe micro analysis (EPMA). The distribution of Si, Mn, Cr and C was obtained by performing a compositional mapping through the samples. The specimens

were prepared in the same way as for optical and scanning electron microscopy and the same surfaces were investigated (figure 3.3).The length of the samples subjected to EPMA variated from 3 to 8 mm.

The measurements were performed with a JEOL JXA 8900R microprobe using an electron beam energy of 10 keV and beam current of 50 nA employing wavelength dispersive spectrometry (WDS). After background correction relative to the corresponding intensities of reference materials, the chemical composition at each location was determined using X-ray intensities of the constituent elements. The line scans were performed with a step size of 2 µm. Elements C, Si, Cr, and Mn were measured, whereas Fe was obtained by difference.

3.5. X-RAY DIFFRACTION (XRD) MEASUREMENTS

X-ray diffraction was used to investigate phase fractions and most importantly, the fraction of retained austenite in different parts of the trailing arm. The same samples F1, F4, and B4 that were subjected to electron probe microanalysis were prepared for XRD. Specimens were grinded and polished to 1 μm diamond suspension. Retained austenite might probably transform to martensite when a certain amount of strain is applied [62]. For that reason, slow rotation speed and light contrast pressure were used during preparation to minimize the mechanical-induced transformation of retained austenite.

The XRD measurements were performed in the X-ray facilities group of the Materials Science and Engineering department at Delft University of Technology. The retained austenite fraction was determined using a Bruker D8 Discover diffractometer, Eiger-2 500k 2D-detector, and Cu Kα radiation. The diffractometer was operated with a current of 100 μA and an acceleration voltage of 50 kV. The scanning range of 2ϑ was 20° – 150° with a step size of 0.040° 2ϑ counting time per step 2 s. Figure 3.6 illustrates the specimens mounted in a standard sample holder in the diffractometer.

The fraction of austenite was calculated by assuming that the sample consists of two phases: austenite and ferrite (ignoring the presence of carbides). Rietveld refinement was used in the semi-quantification of the retained austenite.

XRD was also used to measure also, the austenite lattice parameter. The interplanar spacing d_{hkl} corresponding to a particular hkl peak can be determined using the well-known Bragg equation:

$$n\lambda = 2d_{hkl}\sin\theta \tag{3.3}$$

where n is the order of reflection, λ is the wavelength of radiation, and d_{hkl} is the lattice plane spacing. θ is the reflection angle corresponding to a particular hkl peak as determined by the Bruker DIFFRAC.EVA software. For cubic crystals, the lattice spacing a_{hkl} can be obtained from the interplanar spacing d_{hkl} through the following relation:

$$a_{hkl} = d_{hkl}\sqrt{h^2 + k^2 + l^2} \tag{3.4}$$

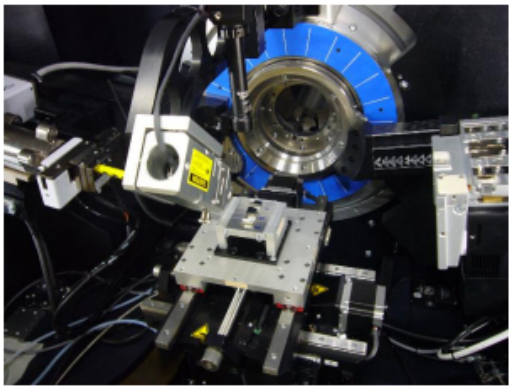

Figure 3.6: Specimens with polished top surface fixed on the standard sample holder.

where a_{hkl} is the lattice parameter and h,k and l are the Miller indices of the lattice plane. For the estimation of carbon in retained austenite, the following empirical relationship was used based on the determined austenite lattice parameter [63]:

$$a_{fcc} = 3.556 + 0.0453x_{\mathrm{C}} + 0.00095x_{\mathrm{Mn}} + 0.0056x_{\mathrm{Al}} \tag{3.5}$$

where a_{fcc} is the austenite lattice parameter in angstrom and x_c, x_{Mn}, x_{Al} corresponds to the weight percent (wt.%) of carbon, manganese and aluminium in austenite.

3.6. HARDNESS TESTING

Hardness testing was applied to all samples after optical and electron microscopy. More specifically, specimens were subjected to microhardness Vickers tests where a diamond indenter is forced into the material's surface with a static load. From the impression of the indenter, the hardness value of the specimen is calculated.

In this research, a Struers Emco-Test DuraScan automatic hardness tester was used and several pre-experimental trials were made to find the optimal static load which could range from 0.01 to 10 kg.

The same areas were investigated as in optical and scanning electron microscopy. A series of measurements (10-30) in a row was done under both 1 and 5 kg in each sample. In transverse and rolling planes measurements were conducted from the bottom of the spring to its surface. From possible variations in hardness values, different microstructures could be identified contributing to explaining possible inhomogeneity.

4

RESULTS

In this section, the results of each experimental procedure described in chapter 3, are presented. With these indications, the microstructure through the silicon-contained spring steel will be elucidated.

4.1. THEORETICAL EVALUATION OF 61SICR7 SPRING STEEL

A thermodynamic study was performed for 61SiCr7 using ThermoCalc Software 2022a (TCFE12 database), mostly to predict phase fractions and critical temperatures and to determine the time-temperature-transformation (TTT) and continuous cooling transformation (CCT) diagrams. The stable phases were limited to ferrite- BCC(A2, A2#), austenite- FCC (A1, A1#), and carbides based on the chemical composition of austempered silicon spring steels. In figure 4.1, the equilibrium phases as a function of the temperature of the silicon spring steel are indicated. The significant amount of silicon (1.63 wt.%) in steel did not delay carbide precipitation and under 760^oC, cementite formation is expected to occur together with the ferrite-BCC phase. Under 300^oC, other phases such as M_7C_3 (BCC-A2#2) and M_3C_2 (FCC-A1#2) start to precipitate.

The TTT of the nominal composition of spring steel (Fe-0.60C-1.63Si-0.97Mn-0.48Cr) is illustrated in figures 4.2 and the calculated M_s and B_s from equations 3.1 and 3.2, present insignificant differences with the results from ThermoCalc software.

The mol fraction of carbon in all phases versus temperature and the CCT diagram of the nominal composition are presented in the appendix.

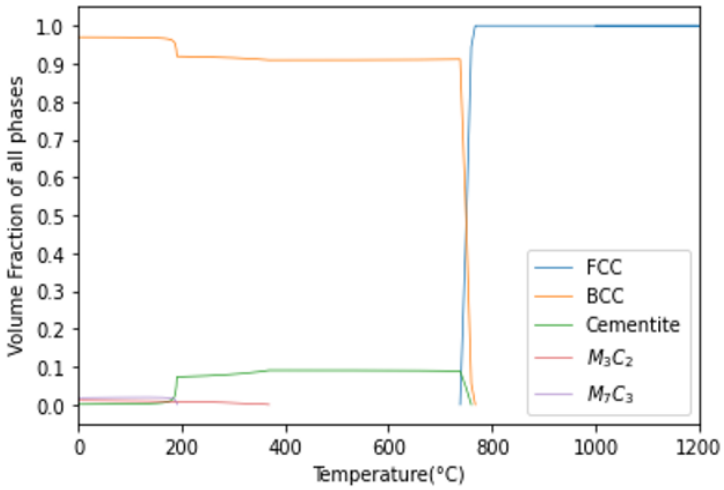

Figure 4.1: Volume fraction of phases of 61SiCr7 versus temperature using ThermoCalc software.

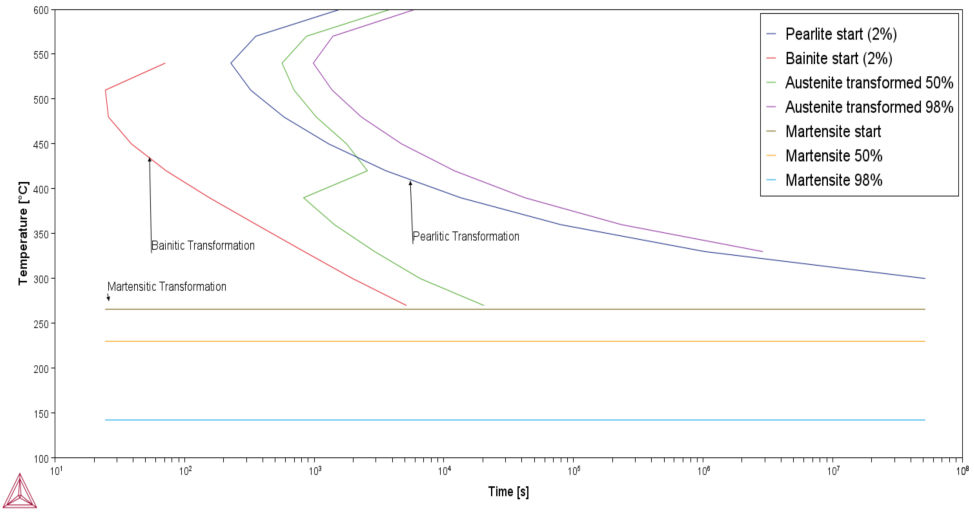

Figure 4.2: Time-temperature-transformation (TTT) of the nominal composition of Fe-0.60C-1.63Si-0.97Mn-0.48Cr using Thermo-Calc software.

4.2. MICROSTRUCTURE OF SPRING STEEL AFTER AUSTEMPERING

The resulting microstructure of the two parts after austempering processing was studied using optical microscopy (OM) and scanning electron microscopy (SEM).

4.2.1. FRONT PART

4.2.1.1. F1

Figure 4.3 (a-e) shows the micrographs after optical microscopy and SEM of the F1 surface of steel specimens from lower to higher magnifications. Since etching with solutions 2% and 5% Nital proved to be difficult to get sufficient contrast between the different phases and grain boundaries, only figures with the optimal resolution are presented.

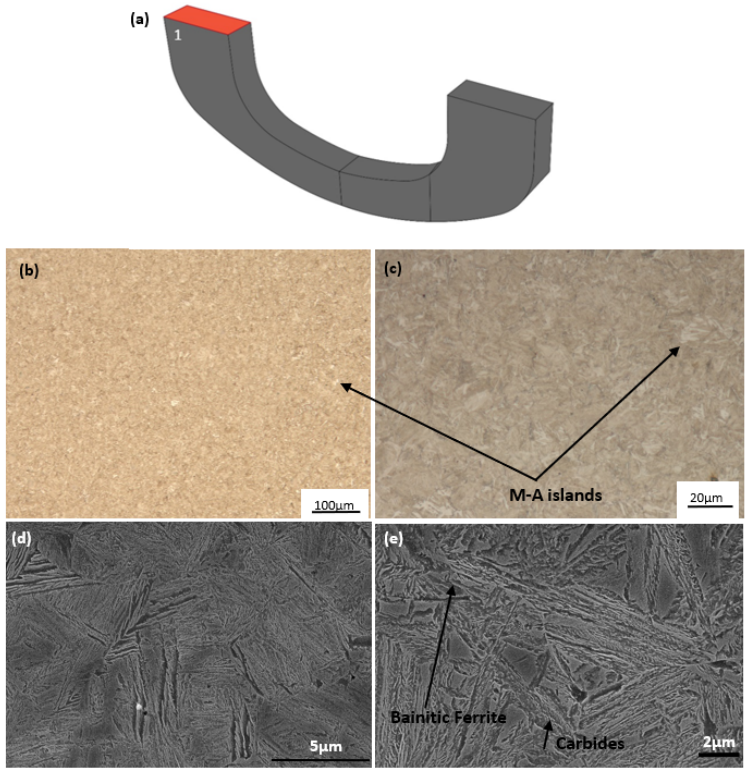

Figure 4.3: (a) Location of investigated surface, (b),(c) optical and SEM micrographs (d),(e) of austempered F1 sample from lower to higher magnification. Bainitic ferrite, carbides, and M-A islands are indicated.

In figures 4.3(c), there are some variations in size and geometry of the white phase which could be identified as blocky retained austenite or else, called M-A islands. The bainitic reaction was incomplete within the time limit of austempering. The identifica-

tion specifically of bainitic ferrite and martensite presented challenges due to similarities in morphology. Finally, between these sheaves, austenitic films are most probably present but, higher magnification characterization methods are needed to determine them. Finally, carbide precipitation was observed in bainitic ferrite.

4.2.1.2. F2

The microstructure of the F2 surface after austempering is presented in 4.4. The location of each micrograph is presented in 4.4(b). Microstructural bands were observed parallel to the rolling direction 4.4 (b). Further experiments were planned to identify the microstructures and alloying element segregation in these bands. In 4.4 (c), the decarbonized layer in the upper area of the trailing arm is presented and is indicated by a black arrow. M-A islands and carbides were observed through the investigated surface.

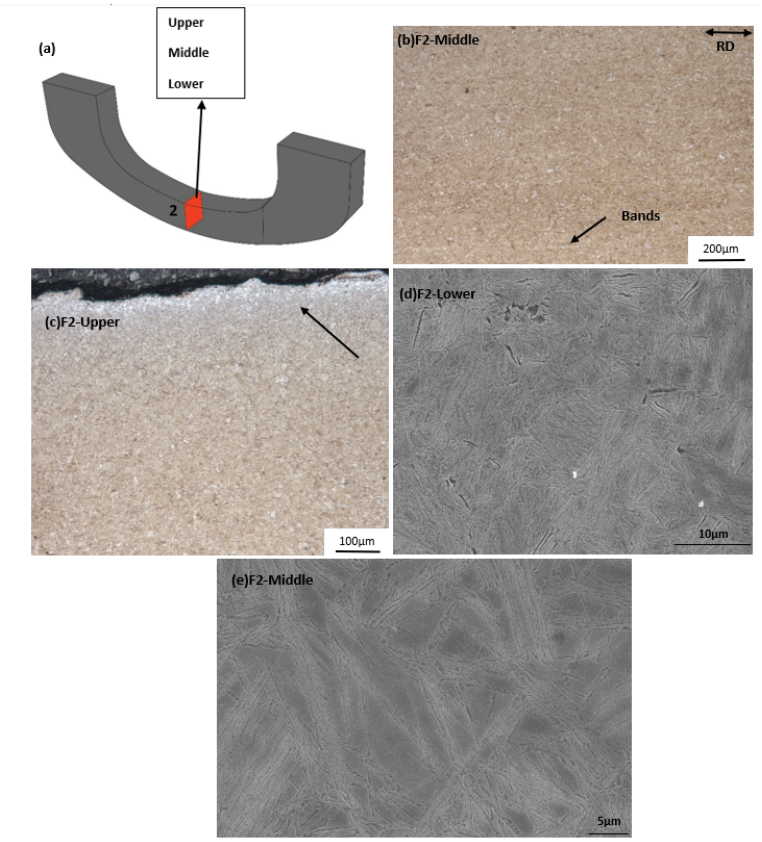

Figure 4.4: (a) Location of investigated surface (b),(c) Optical and (d),(e) SEM micrographs of austempered F2 surface of 61SiCr7 steel. The segregation bands and the decarbonized layer are illustrated in black arrows.

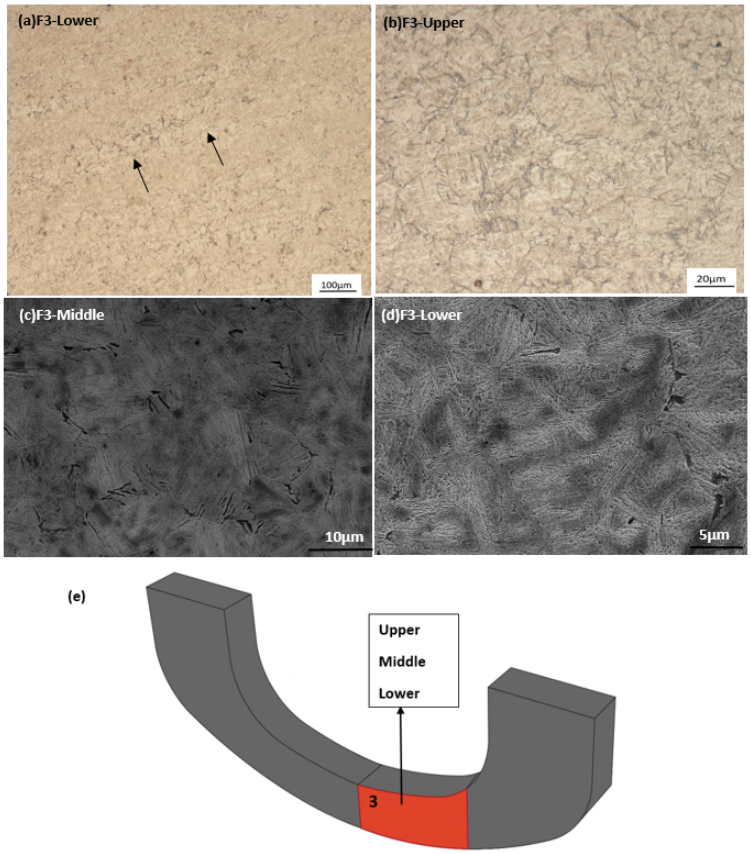

Figure 4.5: (a),(b) Optical and (c),(d) SEM micrographs of austempered F3 surface of 61SiCr7 steel (e) location of investigated surface. The grain coarsening on the banded structure is indicated in black arrows.

4.2.1.3. F3

From figure 4.5 which illustrates the microstructure of the F3 surface, a grain size variation is clear between the banded and non-banded structure. Furthermore, carbides were also formed across the investigated surface.

4.2.1.4. F4

Figure 4.6 illustrates F4's final microstructure. In the upper and lower area, a similar microstructure with the F2 sample was observed. In segregation bands (shown in black arrows), M-A islands were mostly present. More specifically, figure 4.6 (d) illustrates a segregation band in higher magnification, where it could be observed that the appearance of M-A islands is extensive. At M-A islands, carbide precipitation was observed in the middle area (red arrow in figure 4.6(d)), indicating the presence of martensite. Car-

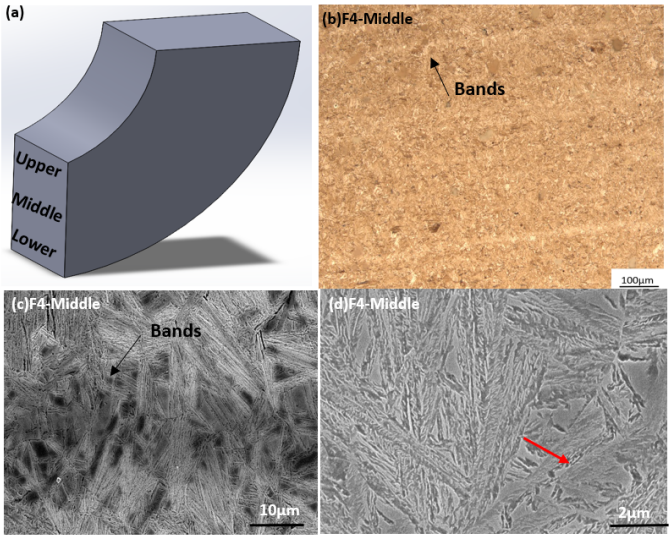

Figure 4.6: (a) Location of investigated surface, (b) optical and (c),(d) SEM micrographs of austempered F4 surface of 61SiCr7. Bands, M-A constituents, and carbides are illustrated in black and red arrows.

bide precipitation was also, observed in bainitic ferrite.

4.2.2. BACK PART

The microstructures in the B1 and B3 samples were similar to the respective samples in the front part. For this reason, the optical and SEM micrographs of these samples are presented in the appendix chapter. The microstructure of the back part is illustrated in a similar way as in the front part.

4.2.2.1. B2

The microstructure of the B2 surface after austempering is shown in figure 4.7. Microstructural bands were formed parallel to the rolling direction and M-A constituents were also, identified in this surface (yellow circle). Finer M-A islands were observed in bainitic laths and are indicated by yellow arrows in figure 4.7 (d). Furthermore, carbide precipitation was observed in the upper, middle, and lower areas.

4.2.2.2. B4

Figure 4.8 displays the microstructure of the B4 area. As indicated in figure 4.8(a), the material showed a significant microstructural banding also, in this investigated surface. The presence of M-A islands in segregation bands was not as significant as in the F4 sample (figure 4.8(d)).

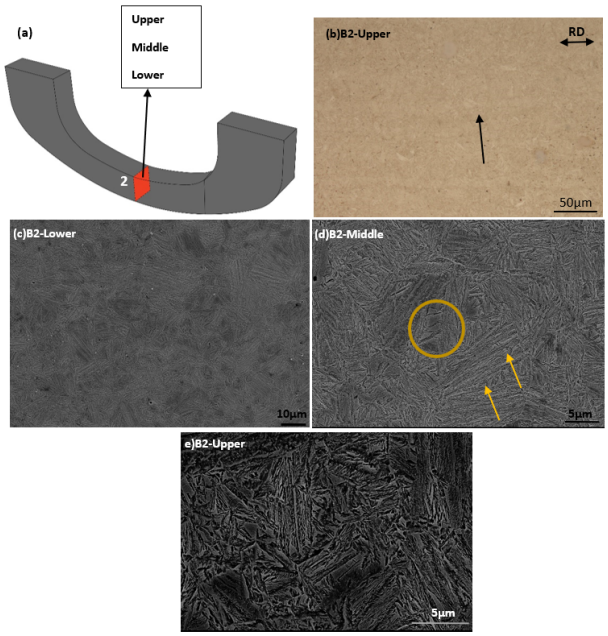

Figure 4.7: (a) Location of B2 surface on the back part of trailing arm, (b) optical and (c),(d),(e) SEM micrographs of B2 surface of austempered 61SiCr7 steel. Bands and the fine M-A islands are indicated in black and yellow arrows respectively. Coarse M-A islands are presented in a yellow circle.

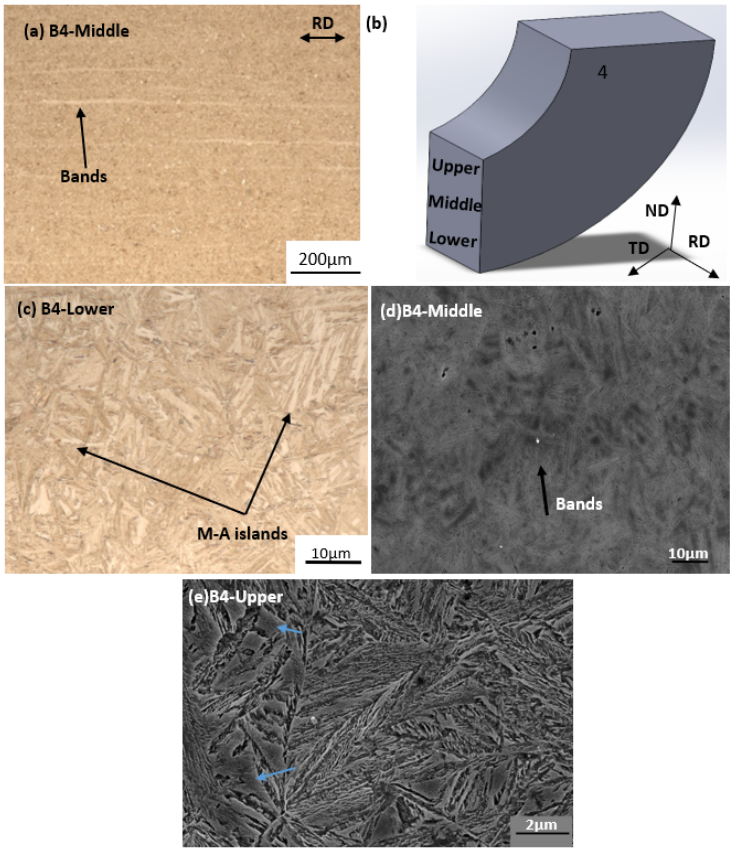

Figure 4.8: (a),(c) Optical micrographs, (b)location of B4 surface, and (d),(e) SEM micrographs of austempered B4 surface of 61SiCr7. Bands and M-A islands are indicated in black arrows. Carbide precipitation in M-A islands is specified in blue arrows.

In this sample also, carbide precipitation in M-A islands was shown as indicated in blue arrows in (figure 4.8(e)).

To conclude, in all investigation surfaces, M-A constituents and carbides were present in different sizes. However, the banded structure was only observed in transverse planes in both the back and front parts. The bainitic ferrite microstructure illustrated in all investigated areas could be considered as lower bainite due to the low treatment temperature and the carbide precipitation. However, further investigation should be conducted to identify this precipitation.

4.2.3. M-A ISLANDS SIZE

As mentioned in the previous section, during isothermal heat treatment, M-A constituents were observed at every investigated surface of both parts. The analyse of the M-A island distribution size in both parts could contribute to explaining the microstructural heterogeneity of spring steel. These were made in the B2, B4, F2 and F4 sample as were the samples where intense presence of M-A constituents was observed. The M-A islands size was measured in the upper, middle and lower area of the samples. The distribution of M-A constituents for both parts in surfaces two and four are illustrated in figure 4.9 where the probability of detecting different size M-A islands is calculated.

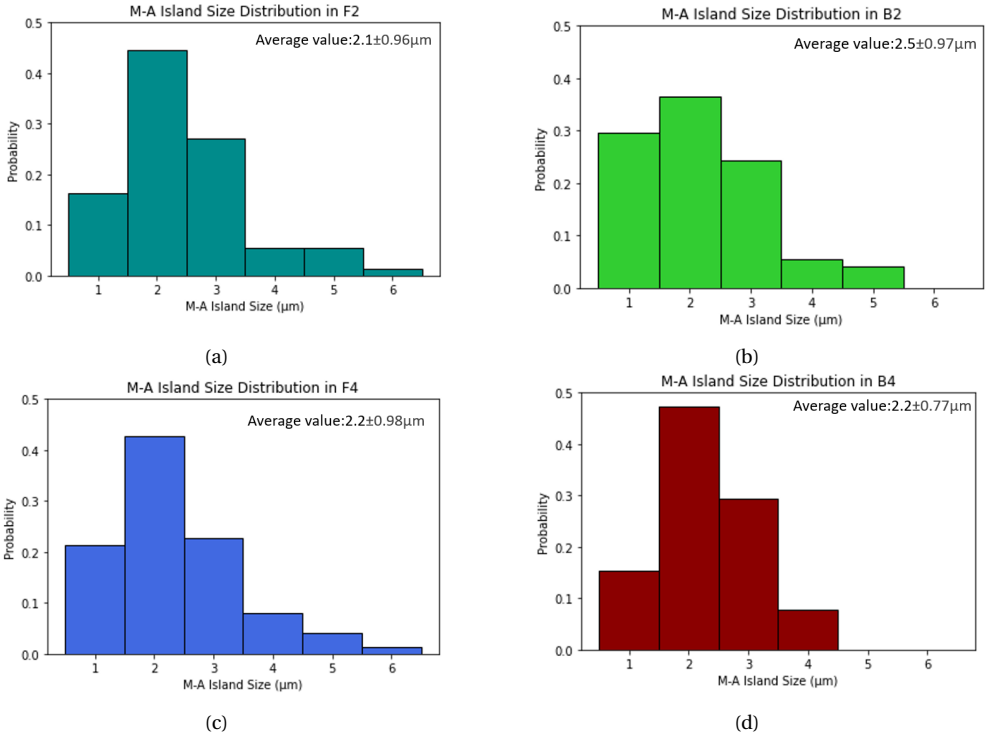

Figure 4.9: Histograms of M-A Islands size distribution of (a) F2,(b) B2,(c) F4 and (d) B4 samples of both back and front parts of austempered 61SiCr7 spring steel. The average value of M-A island size and standard deviation for each sample are presented.

According to the results, the average size of M-A constituents in all investigated surfaces was between 2.0-2.5 μm. However, the distribution of islands is more wide in F2 and F4 surfaces compared to the other surfaces based on the standard deviation. Furthermore, observing coarse M-A islands (over 3.5 μm) is more probable at these surface which could be justified by the intense formation of segregation bands.

4.3. PRIOR AUSTENITE GRAIN SIZE (PAGS) DISTRIBUTION

In figure 4.10, the grain size distribution of prior austenite of both parts are presented. The calculations were applied in similar way as in the measurements of M-A islands in well etched figures using SEM tools. The same samples were used and the PAGS was measured in the upper, middle and lower area of the samples. In the back part, the dis-

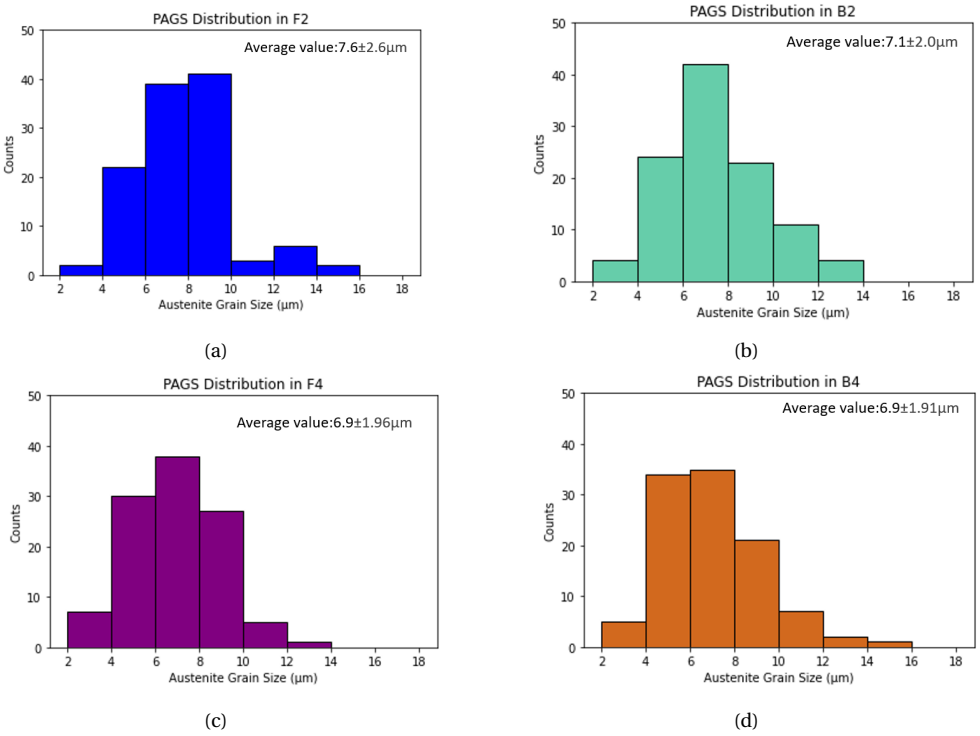

Figure 4.10: Histograms of PAGS distribution of (a) F2,(b) B2,(c) F4 and (d) B4 samples of both back and front parts of austempered 61SiCr7 spring steel.

perse of grains is more right-skewed compared to the front part which could be correlated with the lower thickness of the back part. On the F2 surface, the probability of forming coarse grains (over 12μm) was the highest reaching 7.8%. On the contrary, in the F4 area, the formation of coarse grains was restricted and in B2 and B4, its value was 3.7% and 2.8% respectively.

The F4 and B4 samples presented the same average value but the F4 had a slightly wider distribution due to a higher standard deviation. It was observed that there is no significant difference in the average grain size.

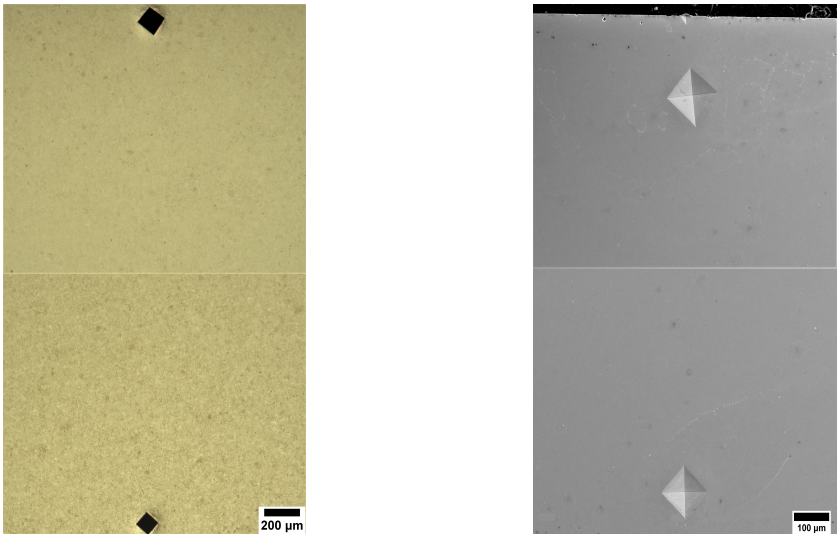

(a) (b)

Figure 4.11: Locations of the EPMA measurement of austempered 61SiCr7 indicating the marked analysis area of B4, using (a) optical microscopy and (b) scanning electron microscopy. The same procedure was followed for F4.

4.4. ELEMENTAL DISTRIBUTION

Electron probe micro analysis (EPMA) was performed to comprehend and compare how elements are distributed in specimens from different parts of the spring and with differences in thickness. More specifically, in B4 and F4 specimens where the number of bands was significantly higher (for both parts) compared to other specimens, two indentations were executed using microhardness testing to mark the analysis area where the banded structure is located in the sample. The indentation of the area was made by tripling the distance between the bands as the near region is deformed after indentation and thus it will influence the EPMA measurements. Figure 4.11 shows this investigation area in this area marked by indents, optical and scanning electron microscopy were performed also.

Table 4.1 presents the elemental distribution of F1, F4, and B4 samples along a line between indents. In specimens F4 and B4, high levels of silicon (over 1.6 wt.%) and manganese (over 0.9 wt.%) were observed. Alloying elements concentration presents higher variations in F4 than in B4 as presented in table 4.1. Silicon was found to segregate together with manganese and chromium. The higher carbon content compared to base composition indicates that indeed carbides precipitated and austenite was not homogeneously carbon enriched as coarse M-A constituents were detected after austempering.

In figures 4.12, 4.13 and 4.14, the distribution of elements Si, Mn, Cr, and C along the F1, B4, and F4 samples are presented respectively together with the B_s and M_s variations and the SEM micrograph of the corresponding area. The temperatures were calculated

Table 4.1: Distribution of alloying elements along F1, B4 and F4 samples of austempered spring steel 61SiCr7

	F1 (wt.%)	**F4 (wt.%)**	**B4 (wt.%)**
C	0.5-0.7	0.60-0.90	0.60-0.80
Si	1.60-1.70	1.30-2.20	1.40-1.90
Mn	0.90-1.10	0.90-1.75	0.90-1.30
Cr	0.45-0.55	0.30-0.80	0.40-0.70
Fe	Balanced	Balanced	Balanced

using equations 3.1 and 3.2, considering the measured contents of Mn, Cr, Si, and C from EPMA results. It is seen that the variations in Si, Mn, and Cr concentrations coincide with the microstructural bands in B4 and F4 samples. For each specimen, the following was observed:

- For the F1 sample, the elemental distribution is homogeneous except for some peaks which correspond to the presence of M-A islands. These constituents showed higher content of manganese and chromium compared to the whole surface. The carbon profile is distributed very close to its nominal composition. B_s and M_s temperatures were close to the ones of nominal composition.

- In the B4 sample, a peak of silicon, manganese, and chromium was observed (3060 μm) and carbides did not precipitate in this area as carbon is more homogeneously distributed. Mn and Cr presented 30% and 24% higher concentrations than the nominal while Si reached up to 17%. The average band thickness was 8.4 ±0.1 μm. In the area rich in Mn/Cr (3560-3570 μm), bainitic ferrite starts to form at lower temperatures compared to the F1 sample.

- In the F4 sample, the distribution of substitutional elements presented the highest variation. In the microstructural band (17.2 ± 0.3 μm), Cr and Mn presented the strongest segregation also, with 75% and 64% respectively higher concentrations than the nominal composition and Si 37%. However, carbon's concentration was only 7% higher indicating that carbon was not attracted in Mn- and Cr-rich regions. The sensitivity of B_s in local chemical composition is evident even if its values are above the austempering temperature.

It is clear from the plots that F4 presented greater elemental variations compared to B4 and F1 samples which could be attributed to the higher thickness chemical segregation bands.

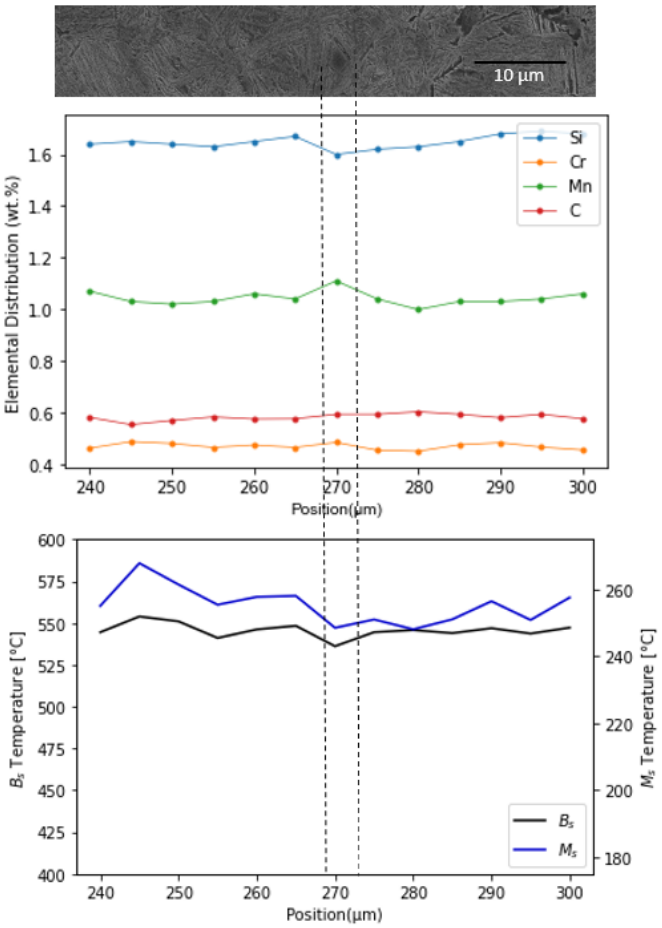

Figure 4.12: Distribution of Si, Mn, Cr, and C along the F1 sample. The normal direction (ND) of the specimens is vertical to the horizontal axis.

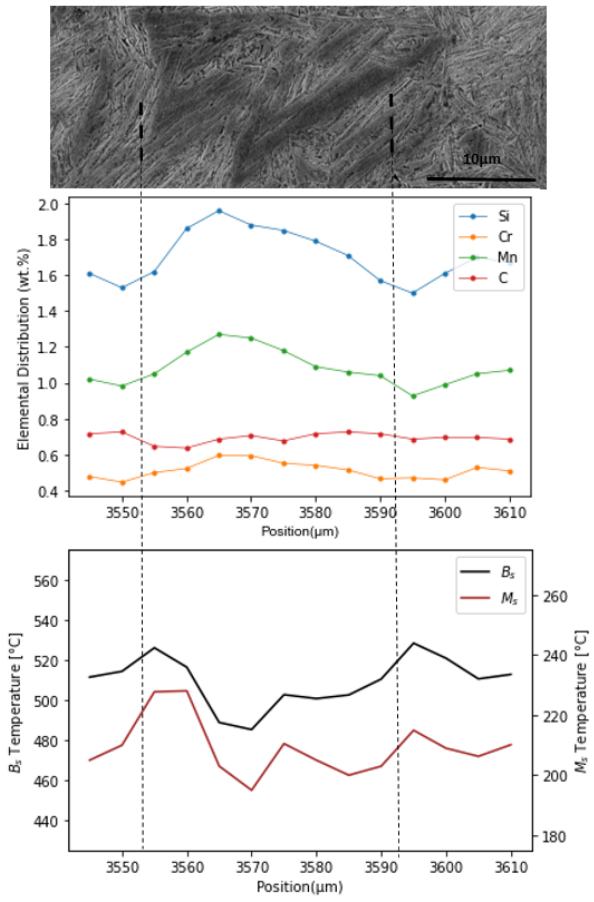

(a)

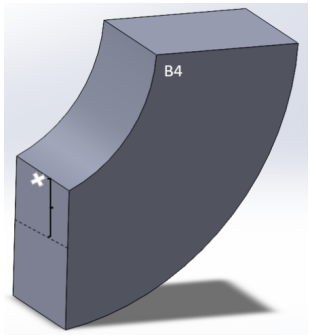

(b)

Figure 4.13: (a) Distribution of Si, Mn, Cr, and C along the segregation band of B4 sample (b) Location of segregation band is marked with a dotted line and with an X, the (0,0) point is indicated. The normal direction (ND) of the specimens is parallel to the horizontal axis.

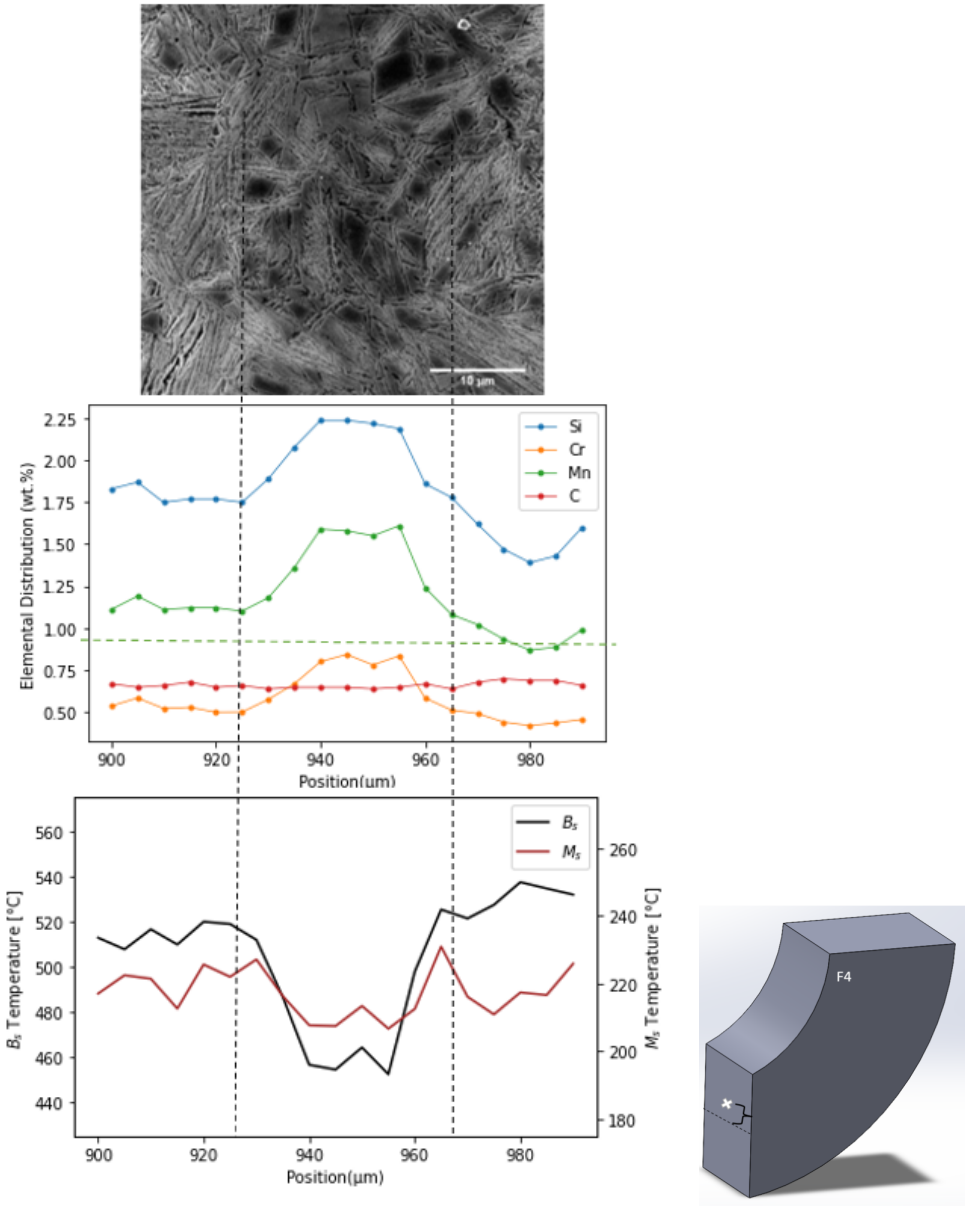

(a) (b)

Figure 4.14: (a) Distribution of Si, Mn, Cr, and C along the segregation band of F4 sample (b) Location of segregation band is marked with a dotted line and with an X, the (0,0) point is indicated. The normal direction (ND) of the specimens is parallel to the horizontal axis.

4.5. VOLUME FRACTION AND LATTICE PARAMETER OF RETAINED AUSTENITE BY XRD

The retained austenite fraction in specimens F1, F4, and B4 was measured using XRD. The diffractograms for all samples are summarized in figure 4.15. The austenite peaks are at 2Theta angles of approximately 45, 65, 85, 98, and 115 degrees and the most contributing peaks were identified from the study of Jatczak Chester who investigated retained austenite's measurements by XRD in steel and from ASTM standard for the X-Ray determination of retained austenite [62][64].

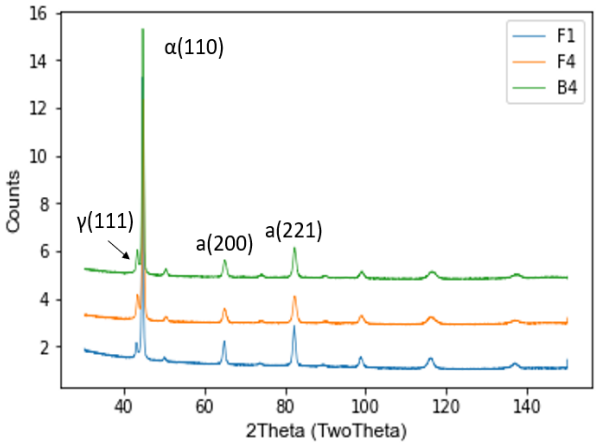

Figure 4.15: Diffractograms of F1, F4 and B4 samples of 61SiCr7 spring steel after austempering for 1 hour where α=ferrite and γ=austenite.

In figure 4.16, the volume fraction of ferrite and austenite for both back and front parts after austempering are shown. Since bainite and martensite have similar crystallographic orientations, they can not be distinguished by XRD. Thus, the volume fraction of ferrite represents both phases. The F1 sample (normal plane of the front part) presents a lower amount of RA at room temperature compared to the other two samples. The fraction of RA measured by XRD may be lower than reality as polishing can cause mechanically-induced transformation of RA.

The lattice parameter and carbon content of austenite (equation 3.5) were calculated and the results are shown in table 4.2. The lattice expansion associated with carbon enrichment of austenite is higher at the F1 sample even though it presented a lower fraction. The austenitic phase in the F4 sample presented a slightly higher carbon content compared to sample B4 even though they contained the same amount of RA.

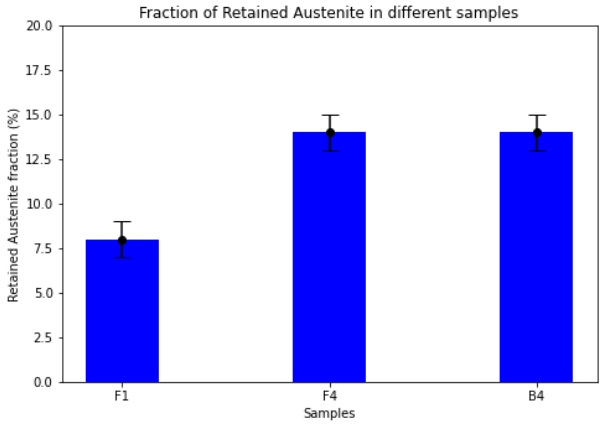

Figure 4.16: Fraction of retained austenite and ferrite in F1, F4 and B4 after austempering based on XRD measurements.

Table 4.2: Lattice parameter and the average carbon content of austenite in F1, F4 and B4 samples of 61SiCr7 after austempering based on XRD measurements.

Sample	Lattice Parameter (nm)	Carbon Content in Austenite (wt.%)
F1	0.3633±0.00009	1.667±0.017
F4	0.3619±0.00007	1.359±0.018
B4	0.3614±0.00006	1.262±0.018

The determination of phase fractions in different investigation areas of both back and front parts could contribute to explaining different microstructural characteristics present through the trailing arm and later how they could affect mechanical behavior such as strength and elongation.

4.6. HARDNESS PROFILE

As mentioned in chapter 3, microhardness measurements were performed to obtain an indication of microstructural variation through the spring steel. The microhardness results (HV5) are summarized in figure 4.17 where the mean hardness value for each investigated area for both back and front parts is displayed. The error bar represents the standard deviation in each investigated surface.

After austempering both parts of the trailing arm indicated high hardness values over 450 HV. However, it is clear from the graph that the back part presented greater hardness in all investigated areas except on the second surface where the front part exhibited slightly higher hardness (1%). The greater difference between the two parts (24%) was observed in the first area and the highest mean hardness value (614 HV) was obtained in the third area of the back part. The presence of wider microstructural distribution in

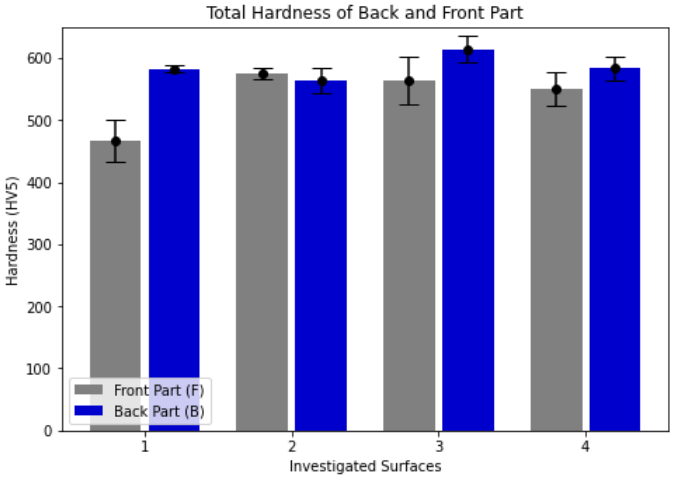

Figure 4.17: Micro-hardness mean values (HV5) of all investigated areas of silicon spring steel after austempering.

the front part is reflected in the standard deviation of hardness measurements which is higher than in the back part.

Figure 4.18(i) illustrates the hardness evolution (HV1) of B2 and F2 from the lower to the upper region of the spring steel together with the location of the measurements in both samples and micrographs of high (610HV for B2 sample and 590HV for F2 sample) and low (550 HV for B2 sample and 590HV for F2 sample) testing values. The color of the scatters corresponds to the respective lines indicating the location of measurements in figure 4.18(ii). It is clear from the plot that the B2 sample presented more heterogeneity in hardness values (except in upper and lower areas) compared to the F2 sample. In the latest one, a small scattering was detected near the upper area. When using a lower load in hardness measurements, greater variations were observed. However, a more precise idea of microstructure variation through the samples is obtained. The error of each hardness measurement was considered as the difference between the two diagonals of each indentation and it fluctuated between 1-2 %.

Hardness distribution (HV1) through B4 and F4 samples are presented similarly in figure 4.19. In these cases, measurements followed a similar trend. Moreover, in the F4 area, fluctuations were observed throughout the sample.

From the hardness distribution through the samples and SEM micrographs, it could be concluded that the high hardness values may be attributed to the presence of M-A islands. However, due to the fine scale of micrographs with indentations, lower load hardness measurements are needed to determine the hardness contributions of the individual constituents.

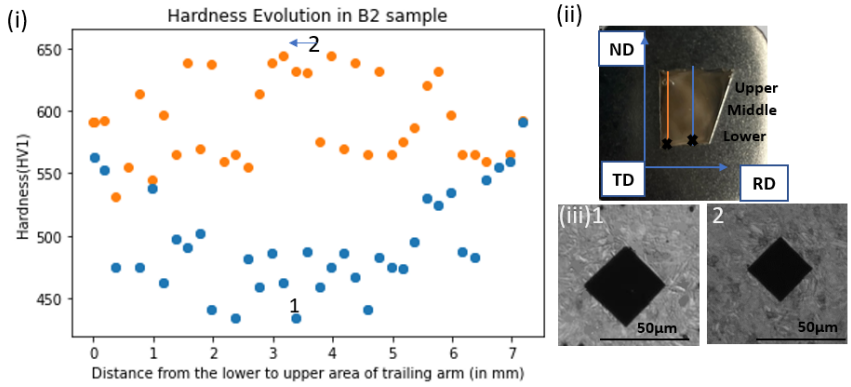

(a)

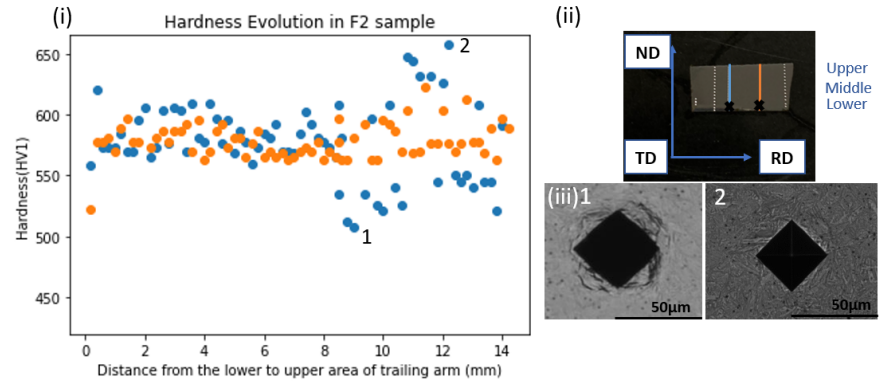

(b)

Figure 4.18: Micro-hardness profile (HV1) of (a)(i) B2 & (b)(i) F2 samples of 61SiCr7 with respect to the distance from the lower to the upper area of the trailing arm. (ii) location of measurements and with an X the (0,0) point is indicated (iii) micrographs of high and low hardness values in both samples. The normal direction (ND) of the specimens is parallel to the horizontal axis.

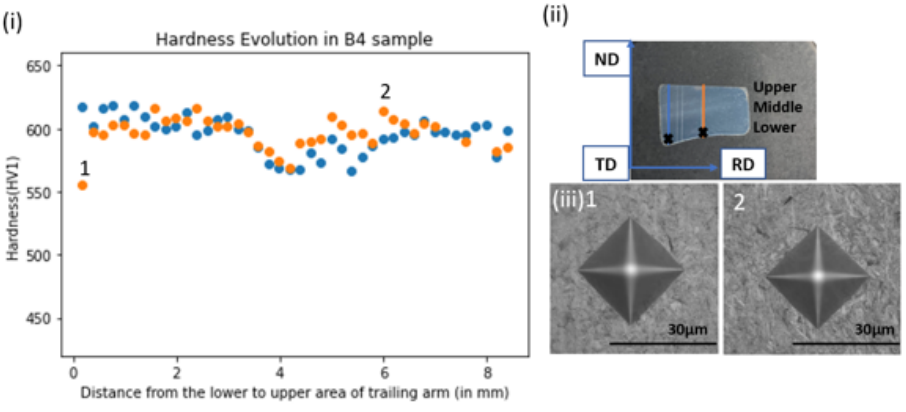

(a)

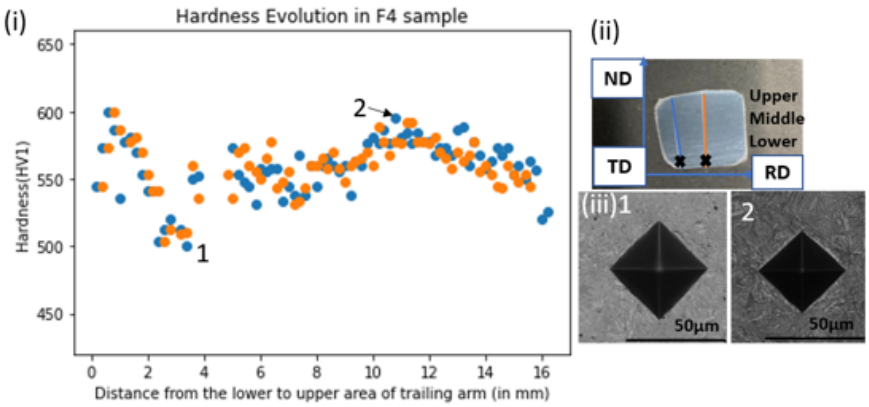

(b)

Figure 4.19: Micro-hardness profile (HV1) of (a)(i) B4 & (b)(i) F4 samples of 61SiCr7 with respect to the distance from the lower to the upper area of the trailing arm. (ii) location of measurements with an X at the (0,0) point is indicated (iii) micrographs of high and low hardness values in both samples. The normal direction (ND) of the specimens is parallel to the horizontal axis.

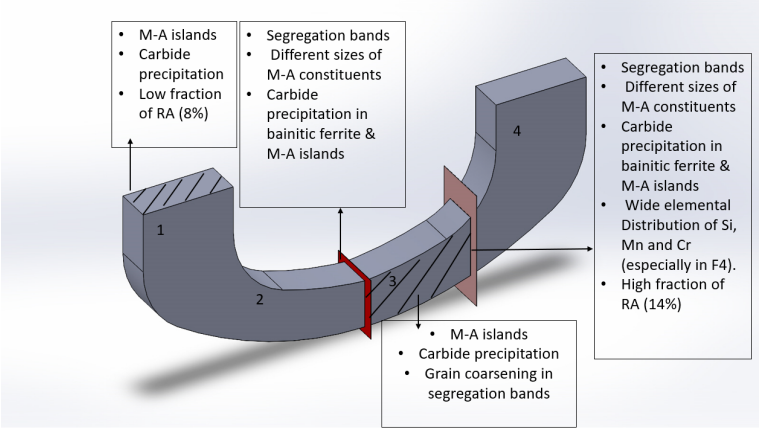

Figure 4.20: Summary of the results in the back and front parts.

4.7. SYNOPSIS OF THE RESULTS

In the following table, the results presented in the previous sectors are summarized in figure 4.20 for the back and front parts to be discussed in the following chapter.

Figure 4.21 presents the scheme of the expected and final microstructure after austempering applied in silicon spring steel. More specifically, the microstructural characteristics developed in an austenite grain, are summarized and the inhomogeneity of the steel is illustrated.

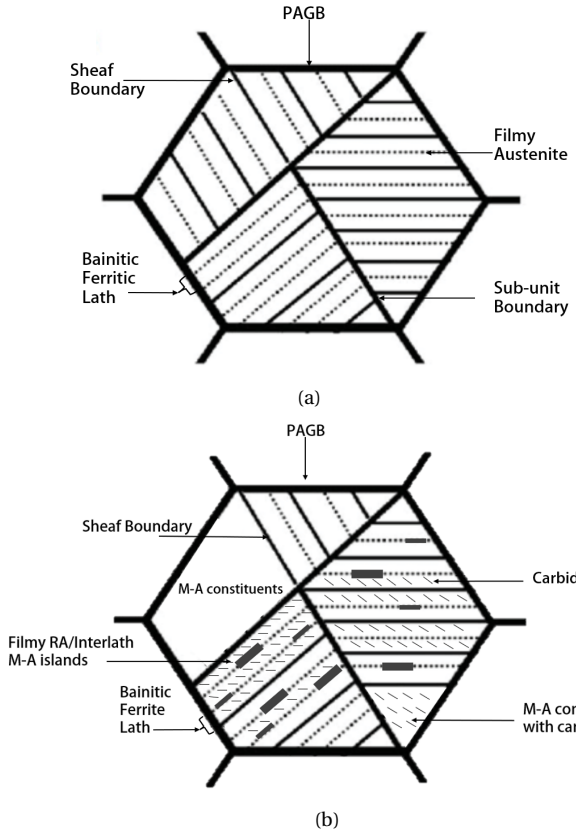

Figure 4.21: Schematic representation of (a) expected carbide-free bainitic microstructure and (b) final microstructure of 61SiCr7 after austempering with PAGB = prior austenite grain boundary, RA = retained austenite and M-A islands= Martensite-Austenite islands.

5

DISCUSSION

In this chapter, the microstructural characteristics of the two parts of the trailing arm are compared to indicate the microstructural heterogeneity. Then, these results are correlated with the hardness, X-ray diffraction (XRD), and electron probe microanalysis (EPMA) measurements to identify the reasons that lead to microstructural variations. Finally, the effect of the microstructural heterogeneity on spring steel's properties is discussed.

5.1. COMPARISON OF THE MICROSTRUCTURE AT THE FRONT AND BACK PART OF THE TRAILING ARM

The microstructure of the investigated spring steel before heat treatment was pearlitic. During austenitization, the material obtained a fully austenitic microstructure. After austempering, bainitic ferrite, M-A islands, and carbides were observed in the different parts based on local chemical composition and temperature.

5.1.1. MARTENSITIC-AUSTENITIC CONSTITUENTS

As explained in chapter 4, the microstructure after austempering of silicon spring steel was studied by optical and scanning electron microscopy (SEM). In the back and front parts, bainitic ferrite formed during austempering together with carbides. M-A islands were observed. The different locations of M-A islands are displayed in figure 5.1. They were located in the boundaries of bainitic ferrite laths (a) and also, next to the prior austenite grain boundaries (b). The intragranular constituents are more elongated compared to the ones next to the PAGB.

To investigate the origin of the M-A constituents and the differences in bainitic ferrite's kinetics through the spring, the TTT diagrams were calculated for the B4 and F4 samples using ThermoCalc software. The TTT curves of the formation of 2% bainite of the B4 and F4 samples are displayed in figures 5.2 and 5.3 at the specific banded region as illustrated in figures 4.13 and 4.14 respectively. The bainite formation started at lower

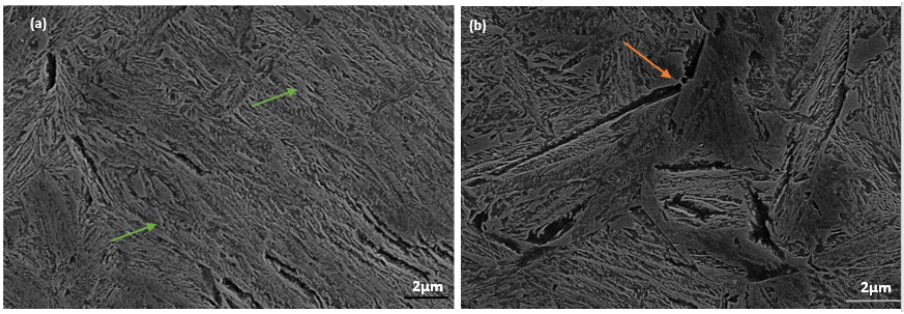

Figure 5.1: Location of M-A constituents in the F4 sample in the upper area of the spring steel (a) in bainitic ferrite's lath boundaries (indicated by green arrows) and (b) in PAGB (indicated by orange arrows).

temperatures at regions with high content in substitutional (Si, Mn, and Cr) elements (HCSER) than with the nominal composition. For both samples, bainite formation is not expected at HCSER during austempering and the longest kinetic delay is observed in the F4 sample which is in the range of 800-1000 seconds.

At regions with low content in substitutional elements (LCSER), bainite formation will be faster for both the back and front parts. In the F4 sample, the chemical composition of substitutional elements in these regions is lower compared to the B4 sample which results in a higher B_s temperature. The transformation kinetics predicted by ThermoCalc implies then that the probability for bainite formation may be greater at the F4 sample at LCSER.

Since in XRD measurements, the peaks BCC include both the bainitic ferrite and martensite, a distinction between the two phases could be made from the hardness measurements. B4 presented higher average hardness (595 HV1 ± 9) than the F4 sample (557 HV1 ±20) which indicates that more martensite in this sample was formed during quenching.

These results together with the SEM observations, hardness measurements, and segregation profile from EPMA results indicate that in highly segregated regions in both front and back parts, M-A islands are the dominant microstructure.

The presence of M-A constituents in every sample could be justified by the following points:

- In the F1 sample (normal plane), the fraction of RA was lower than in the B4 and F4 samples. This fact indicates that austempering time was insufficient for the complete decomposition of austenite. The bainitic transformation was incomplete and austenite at the austempering temperature had low carbon content resulting in its transformation to martensite after quenching.

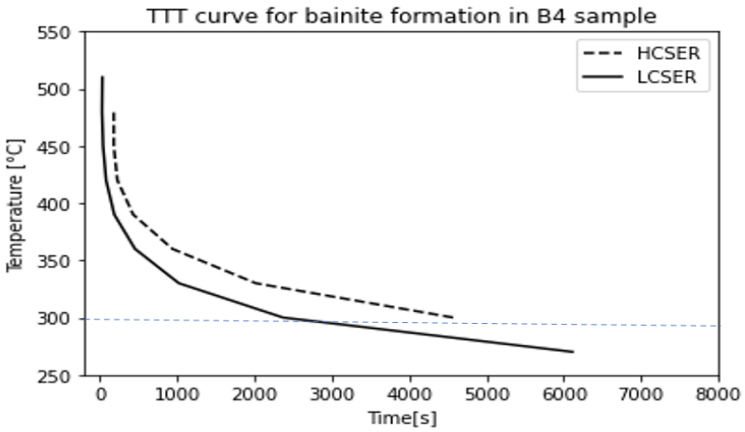

Figure 5.2: TTT curve for bainite formation (2%) in B4 sample in HCSER (Fe-0.69C-1.90Si-1.27Mn-0.59Cr) and LCSER (Fe-0.69C-1.50Si-0.93Mn-0.47Cr). The horizontal dotted line indicates the austempering temperature (300^oC).

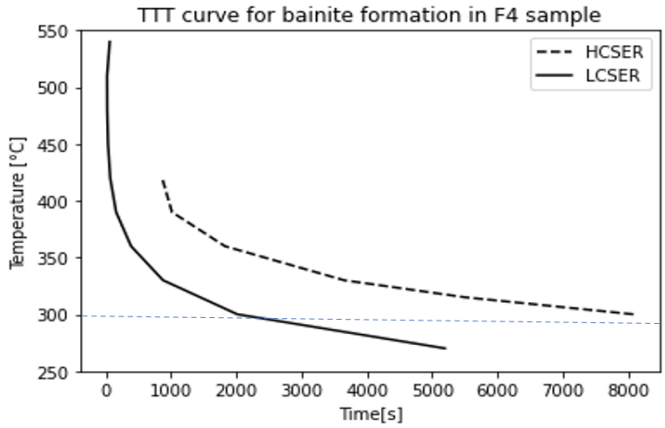

Figure 5.3: TTT curve for bainite formation (2%) in F4 sample in HCSER (Fe-0.65C-2.24Si-1.59Mn-0.8Cr) and LCSER (Fe-0.69C-1.38Si-0.87Mn-0.42Cr). The horizontal dotted line indicates the austempering temperature (300^oC).

- At the bulk of the material (middle area of transversal and rolling planes), thermal gradient, chemical composition, and carbon gradient could explain the presence of M-A islands. The B_s temperature was locally reduced compared to at F1 sample which could be a result of both thermal gradient (lower cooling rate in the middle area from the austenitization to austempering) and chemical segregation. Bainitic ferrite formation will start in this area later than at the F1 specimen and the isothermal holding period could be again insufficient to obtain a full ausferritic microstructure. The effect of chemical segregation in bainitic ferrite kinetics will be analysed in the following sections. Carbon gradient can result in austenite having different carbon contents through the material during austempering. The austenite with low carbon content will transform into martensite during quenching.

The presence of M-A islands due to insufficient isothermal holding time in carbide-free bainitic steel was confirmed by Hofer et al. [43]. Furthermore, the incomplete bainite reaction due to the presence of M-A constituents in spring steel was observed also, by Goulas et al.[9]. These results contribute to a better understanding of the microstructural distribution through the back and front parts of spring steel.

5.1.2. CARBIDE PRECIPITATION

Carbide precipitation in bainitic ferrite was confirmed in every investigated surface in both parts by SEM. In the upper and lower region of the trailing arm, the addition of Si did not suppress significantly carbide formation in bainitic ferrite even though the composition of silicon was higher than 1.5 wt.%. According to the EPMA results, carbides precipitated mainly in regions where carbon concentration was high such as the interface of bainitic ferrite and austenite.

Based on the chemical composition of the steel and the results from ThermoCalc software, the carbides that precipitated, are most probably cementite and/or ϵ and/or manganese and chromium carbides. However, the formation of the latest could not be identified with the present experimental work. Furthermore, there are no clear indications of whether carbide precipitation was more intense in one of the parts.

The formation of carbides could also, explain the low amount (8-14%) of retained austenite. Due to carbide precipitation, less carbon was available to enrich austenite. Consequently, austenite obtains insufficient carbon content to be stabilised resulting in its transformation into martensite during quenching.

Carbide precipitation in high silicon carbide-free bainitic steels was observed also, in the study of Hofer et al. and Timokhina et al. [65] [66].

5.2. ASSESSMENT OF INHOMOGENEITY

The aim of austempering when applied to a silicon spring steel is to obtain a carbide-free bainitic microstructure. The origin of heterogeneity and how thermal gradient, chemical segregation, and carbon gradient cause the formation of a different microstructure are going to be analysed in the following subsections.

5.2.1. THERMAL GRADIENT

The presence of thermal gradient during heat treatment was confirmed by several points. Firstly, three different types of M-A islands were observed through the spring steel and are illustrated in figure 5.4. More specifically:

- **Auto-tempered M-A islands** are constituents where fine carbide precipitation was observed in both parts and could be attributed to the lower cooling rate of the middle area compared to the upper/lower region. Figure 5.5 displays how the cooling rate (C.R.) could variate in different investigation areas after austempering. For the martensite which forms at high M_s temperatures and has a low carbon content, there is time to be tempered during quenching.
- **Less-tempered M-A islands** were observed in F2, F3, F4 and B2, B3, B4 samples between the middle and upper/lower region. Carbide precipitation is not as clear as in the auto-tempered M-A islands due to a higher cooling rate.
- **Carbide-free M-A islands**: observed mostly in the F1 and B1 samples and the HCSER of the front part due to high concentration of Mn and Cr.

Hardness distribution could also indicate the presence of a thermal gradient. Generally, the measurements in the upper and lower area of B2, B4 and F2 were akin, except in the F4 sample. This fact indicates that in these regions, similar microstructural characteristics were present. Through the B4 and F4 samples, more tempered M-A constituents were identified which present lower hardness due to lower carbon content compared to carbide-free constituents. However, since segregation bands were observed, hardness distribution could be attributed also, to chemical segregation.

The heterogeneity in PAGB size could be attributed also, to the thermal gradient. In the bulk of the material, a longer time is needed to reach the isothermal heat treatment temperature and spring steel remains longer at high temperatures where grain growth occurs.

Thermal gradient induces the formation of different microstructural features through the material in the following ways. More specifically, in refined grains ($\prec 5\mu$m) where the grain boundary area is increased, the nucleation sites for bainitic transformation would be augmented. Furthermore, the incubation period for the bainitic transformation depends both on the grain size and the treatment temperature [48]. That leads to the conclusion that in coarse grains where the austempering temperature is lower due to thermal gradient, the incubation period for bainitic transformation will be greater.

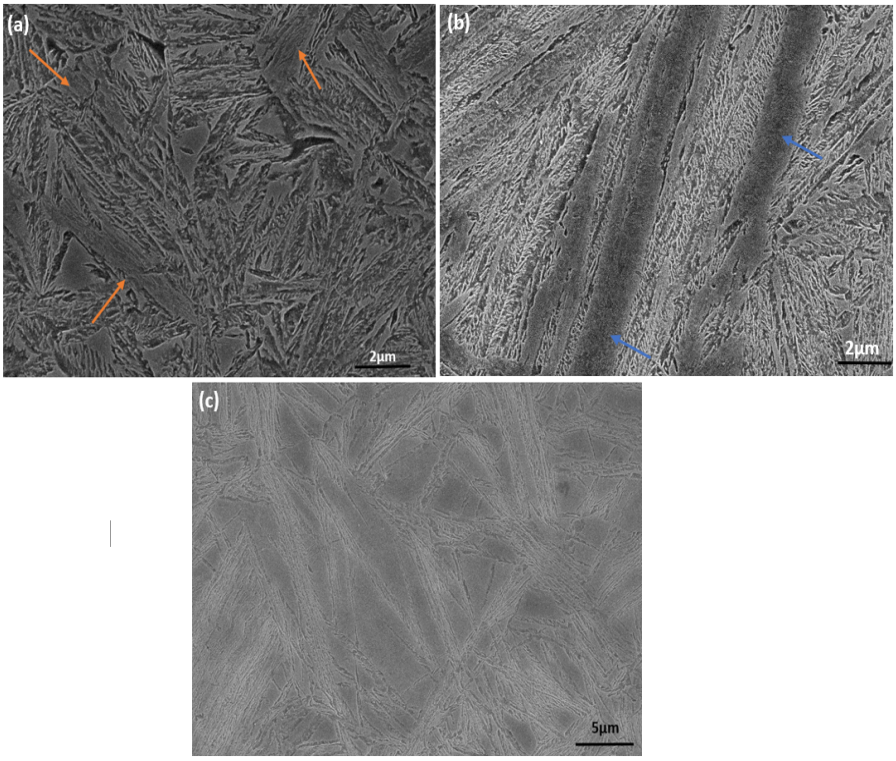

Figure 5.4: SEM micrographs of (a) auto-tempered (b)less-tempered and (c) carbide-free M-A islands in B2, B4, and F2 samples respectively. Auto-tempered and less-tempered M-A constituents are presented with orange and blue arrows respectively.

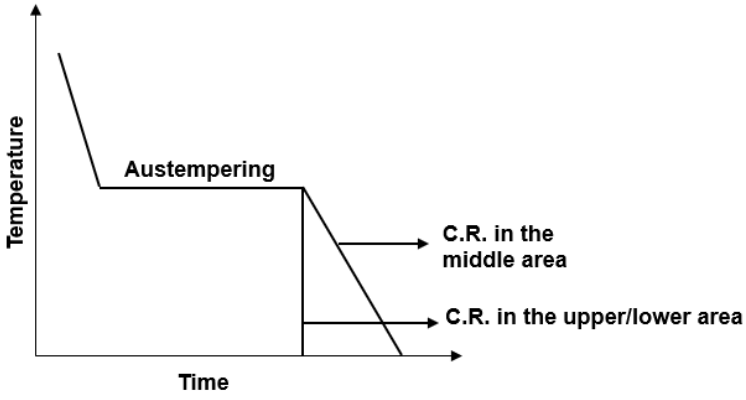

Figure 5.5: Cooling rate (C.R.) variations of different investigation regions after austempering of spring steel.

Thermal gradient effects on hardness measurements were confirmed also, by Tian et al. by both simulation (using fine element model) and experimental validation in a Si-Mn-Cr steel[67]. Similar results were obtained by Matsula et al. that investigated the effects of auto-tempered martensite on the mechanical properties of a Fe-C-Si-Mn-Cr steel [68]. Thermal gradient in steel was confirmed by hardness distribution caused by auto-tempered martensite.

5.2.2. CHEMICAL SEGREGATION

Chemical segregation in banded structures was confirmed using electron probe micro-analysis (EPMA) and could be attributed to the fact that the middle area of spring steel is the last to solidify zone based on figure 2.12 and substitutional elements tend to diffuse in this area causing segregation.

The sensitivity of B_s temperature in local differences in chemical composition is presented together with the segregation profile of the B4 and F4 samples. In the HCSER, the B_s temperature was lower than in the LCSER and closer to the austempering treatment temperature. This results in a lower undercooling in HCSER and consequently, is a lower driving force for bainitic ferrite formation[69].

To understand more in-depth the differences in bainitic ferrite formation, the T_o temperatures were calculated using ThermoCalc software in figure 5.6 for the nominal composition and the HCSE of B4 and F4 samples with the same compositions as in figures 5.2 and 5.3. In dotted lines, the carbon content of austenite in F1, F4, and B4 samples are illustrated. It is clear from the plot, that chemical segregation had, as a result, moving T_o curve to lesser carbon concentrations. The bainitic ferrite formation may be greater in areas with the nominal composition as in HCSER it will cease in lower carbon content if it is considered that the bainitic ferrite forms based on the diffusionless theory.

Based on XRD results, however, in F4 and B4 samples, the same fraction of retained austenite was calculated. This fact indicates that the more intense chemical segregation in the F4 sample did not affect strongly the fraction of RA.

In the F1 sample which has almost the nominal composition, during isothermal heat treatment, carbon content reached values over the T_o curve (thick black dotted line). If it is considered that the bainitic ferrite forms based on the diffusionless theory, in the F1 sample, the bainitic transformation had ceased earlier than in the other two samples. However, in this research, there are no clear indications of whether bainitic ferrite forms based on the displacive or diffusion-controlled theory.
These results could explain the lower fraction of retained austenite in the F1 sample confirmed by XRD measurements.

Caballero calculated also, the T_o curve for carbide-free bainitic steel with higher carbon (0.8 wt.%) compared to 61SiCr7. The curve was sifted to lower carbon contents but the amount of carbon in austenite was similar to this work [58]. Tenaglia et al. investigated also, the amount and carbon content of RA at room temperature after austem-

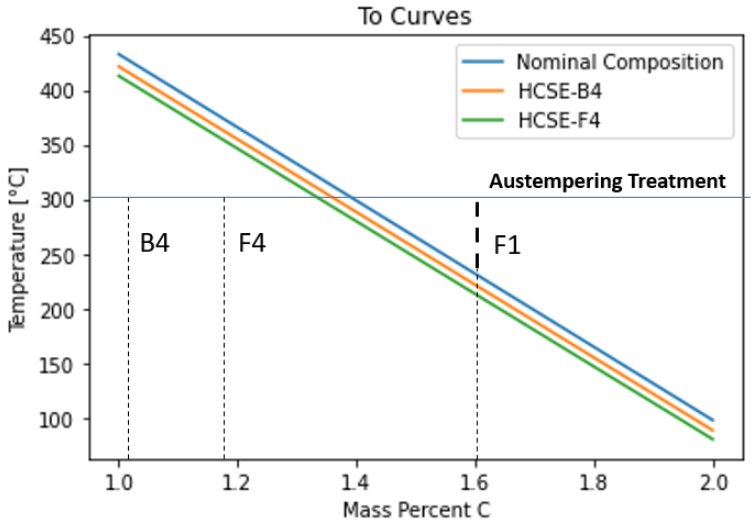

Figure 5.6: The T_o curves of base composition, F4 and B4 samples of 61SiCr7. The dotted lines correspond to the carbon content of retained austenite in every sample.

pering at 300^{o}C for 20-80 min in silicon steel with a lower amount of carbon (0.4-0.45 wt.%) compared to this study. Even though a similar amount of retained austenite was present at room temperature (10-17% and 8-14% at present study), carbon content was less (0.95-1 wt.%) [70]. These results signify that the average carbon content in steel influence significantly, the bainitic formation and the carbon content in austenite and consequently its stability during final cooling.

The slow kinetics of bainitic ferrite in high Mn/Cr regions was also confirmed by the same study [70]. Akin results were obtained by Moralea-Rivals et al. that investigated the complex banding of continuously cooled carbide-free bainitic steel containing a however lower amount of silicon (1 wt.%) and carbon (0.23wt.%) compared to 61SiCr7 [71]. In segregation bands after isothermal heat treatment, high content of chromium and silicon was observed compared to the non-banded structure but manganese's content was lower than the base composition.

These results indicate that Si, Mn, and Cr segregation has a significant effect on the homogeneity of the final microstructure of austempered spring steel.

5.2.3. CARBON GRADIENT

The carbon gradient has a more local effect compared to the thermal gradient (mm) and chemical segregation (μm).

Carbon gradient was confirmed based on SEM results. Figure 5.7 illustrates an M-

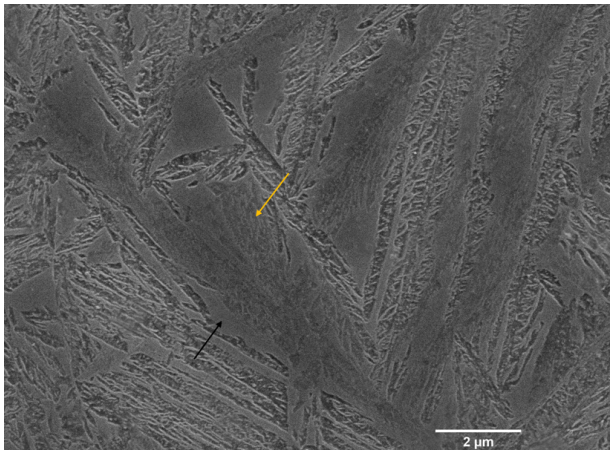

Figure 5.7: M-A island in B4 sample of 61SiCr7 after austempering. High carbon edges and the less carbon-containing of M-A constituent are illustrated with black and yellow arrow respectively.

A constituent at the B4 sample where carbides have started to precipitate towards the center of the island. This fact indicates that in the center of the island, carbon content was lower compared to the edges of the constituent otherwise carbides would not have been formed. In the black arrow, the high carbon edges are presented and in yellow, the less carbon area of the constituent.

The fine M-A islands in the bainitic ferrite's lath boundaries could also, indicate the carbon segregation through the material.

During the austempering treatment and bainitic ferrite formation, there is untransformed austenite in blocky form. At the interface of bainitic ferrite/austenite, austenite at the edge of the block could obtain the carbon content indicated by the T_o curve, hindering bainitic transformation locally. At this point, however, the carbon concentration in the center of the block is relatively low, leading to its transformation to martensite (M-A island).

The carbon segregation could be explained by the limited carbon diffusion in austenite during austempering. For a binary Fe-C system, the distance for carbon diffusion in austenite could be estimated by the equation $x = \sqrt{D_C t}$ with D_c in $m^2\ s^{-1}$ being the diffusivity of carbon in austenite and expressed by Ågren in the following equation and t is the holding time in seconds [72]:

$$D_C = 4.53 \cdot 10^{-7} \left(1 + y_C \left(1 - y_C\right) \frac{8339.9}{T}\right) \exp\left\{-\left(\frac{1}{T} - 2.221 \cdot 10^{-4}\right)\left(17767 - y_C 26436\right)\right\} \tag{5.1}$$

where $y_C = x_C / (1 - x_C)$, x_c being the mole fraction of carbon, and T the temperature in Kelvin. During austempering at 300^oC which is considered the treatment temperature

(300^{o}C) for the material with base composition, for 1 hour, carbon can diffuse a distance of 0.11 μm. In microstructural bands the treatment temperature was lower due to the thermal gradient, and the diffusion distance is even smaller. Moreover, in finer grains, the carbon distribution will be more homogeneous as there will be enough time for carbon partitioning in the whole grain.

All these results indicate that the bainite transformation advances non-uniformly along the different areas of the trailing arm, leading to a heterogeneous microstructure that can be detrimental to the mechanical properties.

5.3. EFFECT OF INHOMOGENEITY IN SPRING STEEL'S PERFORMANCE

The variation of microstructure through the material influences significantly the mechanical behavior of the spring steel. In this section, the impact of microstructural characteristics on the performance of the steel during mechanical loading will be discussed.

This type of steel could present both high strength and ductility. High strength (over 1500 MPa) could be achieved due to the fine bainitic laths and martensite. The fine laths formed during low austempering temperatures which lead to high dislocation strengthening. Ductility is controlled by the amount of softer phase, in this case, retained austenite. Its presence at room temperature could contribute to a pronounced TRIP effect during mechanical loading. Austenite with a high level of carbon (>1.8wt.%C) even at high levels of strain will not transform to martensite [73]. In this study, based on the average carbon measurements in austenite, it is considered that the TRIP effect will occur during mechanical loading of 61SiCr7 after austempering for 1 hour. This fact could contribute to the development of enhanced fatigue properties, important for spring steel.

Stress concentration may be introduced, however, during loading due to the higher hardness of the M-A island, especially in the front part, where the probability that the microstructure consists of coarse M-A constituents is higher. This fact concerns mainly the M-A islands devoid of carbides as they exhibit higher hardness than the auto-tempered martensitic constituents. To confirm this probability, hardness measurements with 0.2 kg load, as shown in figure 5.8 were applied in B4 and F4 samples through the segregation band and bainite ferrite. The results are presented in table 5.1.

Table 5.1: Hardness results through segregation bands and bainitic ferrite

Sample	**Segregation Bands (HV0.2)**	**Bainitic Ferrite (HV0.2)**
B4	640±10	520±6
F4	620±8	540±6

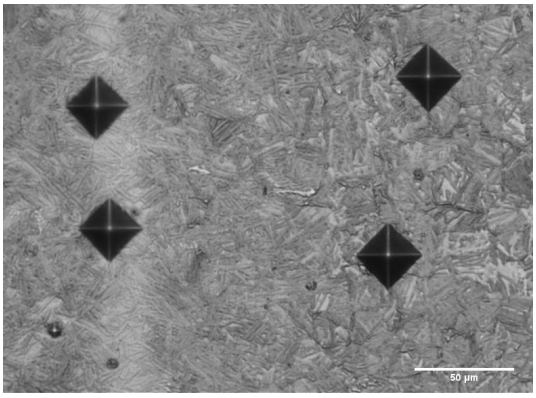

Figure 5.8: Hardness measurements (HV0.2) in segregation bands and bainitic ferrite in F4 sample.

Based on hardness measurements, the trailing arm under cyclic load could potentially fail with a crack initiating from an M-A constituent due to high hardness differences between microstructures. Carbides could be also, a cracking initiation site as they could crack or debond from the bainitic matrix. Similar hardness values in bainitic ferrite were observed by Caballero et al.[34].

Decohesion occurred in the bainitic ferrite/ M-A islands interface of carbide-free bainite during tensile testing [74].

These results indicate that this spring steel could be part of the air suspension system as it presents optimal mechanical properties but the microstructural distribution through the material could affect its final performance.

5.4. SIGNIFICANCE OF THE RESULTS

In every experimental work, final results are affected by a plurality of factors. In this work, results were influenced in the following ways:

- Cutting affected the material as deformation occurred in the near areas causing lower hardness measurements in this area.
- After grinding with silicon carbide papers, some fine carbides remained in the material due to the difficulty to obtain a completely flat surface. Thus, this event affected not only SEM results but also, EPMA as the carbon content may be lower than the one measured.
- Etching 61SiCr7 steel presented a great challenge and consequently, samples were overetched and needed to be prepared again. Grinding multiple times may have caused a reduction in thickness in the banded area as the new investigation surface was closer to the edge of the trailing arm. Hence, in reality, the chemical composition of substitutional elements of the segregation bands might be higher compared to the measurements by EPMA.

- Last but not least, sample preparation and more specifically, polishing may have affected the final amount of RA due to its transformation to martensite when strain is applied.

6

Conclusion and Recommendations

6.1. Conclusions

This thesis aimed to identify microstructural heterogeneity in a forged trailing arm made of silicon-containing spring steel after austempering and explain possible reasons that lead to this microstructural distribution. Bainite's formation was investigated in a conventional, industrially produced high silicon medium carbon spring steel alloy after austempering for 1 hour. Based on in-depth characterization, thermodynamic analysis, and elemental distribution using optical microscopy, SEM, EPMA, XRD, and hardness measurements, an explanation for the formation of different microstructural characteristics in different scales was provided. Experiments were conducted in two different parts of the trailing arm: back (8-12 mm) and front (13-17 mm). Three sources of heterogeneity were indicated for investigating the microstructural distribution: thermal gradient (mm), chemical segregation (μm), and carbon gradient (local effect).

The main conclusions of the study are as follows:

- Bainitic ferrite, M-A constituents, and carbides were the main microstructural features in all investigated surfaces after austempering for 1 hour.
- Thermal gradient, chemical segregation, and carbon gradient affected the microstructural development as follows:
  - **Thermal gradient** was confirmed by the presence of auto-tempered M-A islands and hardness distribution in both back and front parts. The heterogeneity in PAGS that is caused by thermal gradient may lead to non-uniform bainitic ferrite nucleation. Thermal gradient influenced more the microstructure of the front part based on the standard deviation of hardness measurements due to its higher thickness.

  - **Chemical segregation** bands were observed in the middle area of B2,B4,F2 and F4 samples of the trailing arm. In high concentration of substitutional elements regions (HCSER), the bainitic ferrite kinetics was slower in both parts compared to low concentration regions (LCSER) due to lower undercooling which leads to a lower driving force for the transformation. The F4 sample presented more intense chemical segregation than the B4 sample due to HCSER.
  - **Carbon gradient** was confirmed by the presence of auto-tempered M-A islands where the edges of the constituent were more enriched in carbon compared to the center of the island. Carbon diffusion in austenite was limited during austempering (0.11 μm).

- Based on the T_o temperatures, the average carbon of steel and its distribution through the material influences the bainitic ferrite formation and the carbon content of austenite.

- The same fraction of RA (14%) in the B4 and F4 samples and the higher hardness of the back part indicate that the more intense thermal gradient and chemical segregation of the front part did not influence the microstructure as significantly as the carbon gradient.

Nonetheless, fine bainitic laths, martensite, and retained austenite could provide high strength and ductility respectively during mechanical loading making it a promising candidate for a trailing arm.

These results could be used to identify possible challenges for the development of this microstructure in large-scale applications and are briefly analysed in the appendix chapter.

6.2. RECOMMENDATIONS

The recommendations for this study concern both the experimental procedures for the deeper analysis of this work and the new proposals for future work. Further analysis of this work could include:

- Electron Backscatter Diffraction (EBSD) could be used in austempered samples for precise phase identification and distinguishing bainitic ferrite and martensite. Also, EBSD could be used for the quantification of M-A islands and PAGS and compared with this study.

- Characterization techniques such as saturation magnetization could be considered for more precise determination of the retained austenite in austempered samples at room temperature. Another technique could be EBSD but sample preparation could affect also these results.

- Dilatometry measurements could be conducted in not austempered samples to investigate the effect of different cooling rates in microstructure by monitoring

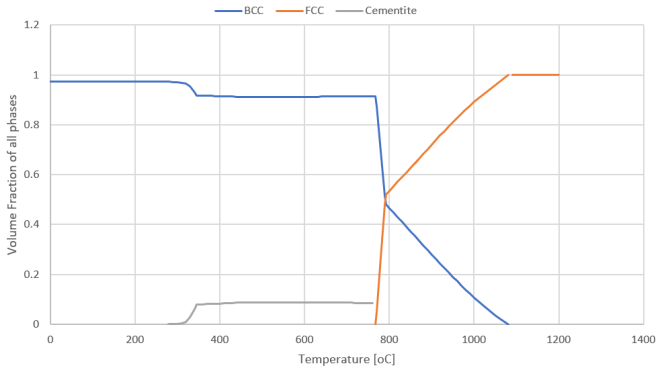

Figure 6.1: Volume Fraction of all phases of proposed silicon spring steel to minimize carbide precipitation.

dimensional changes of the material as a function of temperature. Furthermore, the precise incubation period for bainitic transformation could also be measured.

- Transmission Electron Microscopy (TEM) could be used to determine filmy austenite, the thickness of bainitic ferrite's laths, and possible chromium and manganese carbide precipitation.
- Hardness measurements with a low load (< 1 kg) could be conducted to obtain a precise relation between hardness and microstructure.

As future work for this specific material, the following could be added:

- Low-cycle fatigue tests could be conducted to obtain a more accurate idea of the material's performance.
- Fractography in fatigue or tensile tests using SEM could also be applied to investigate the microstructure that leads to crack initiation and propagation.
- Different heat treatment parameters could be used such as holding time and compare them with this work results. Longer holding time at austempering temperature could contribute to austenite's enrichment by carbon.
- Figure 6.1 illustrates the volume fraction of all phases for a material proposed (Fe-0.6C-2.5Si-0.97Mn-0.48Cr-1.5Al). The addition of aluminium (1.5 wt.%) and the increase in silicon content could contribute to the further delay of carbide precipitation.

BIBLIOGRAPHY

[1] G. Napoli, S. Mengaroni, M. Rallini, L. Torre, and A. Schino, "Interrupted quenching in high carbon forged components," *Metalurgija -Sisak then Zagreb-*, vol. 56, p. 337, Nov. 2017.

[2] R. Kuziak, R. Kawalla, and S. Waengler, "Advanced high strength steels for automotive industry," *Archives of Civil and Mechanical Engineering*, vol. 8, no. 2, pp. 103–117, Jan. 2008, ISSN: 16449665. DOI: 10.1016/S1644-9665(12)60197-6.

[3] Z. Dai, H. Chen, R. Ding, Q. Lu, C. Zhang, Z. Yang, and S. van der Zwaag, "Fundamentals and application of solid-state phase transformations for advanced high strength steels containing metastable retained austenite," *Materials Science and Engineering: R: Reports*, vol. 143, p. 100 590, Jan. 2021, ISSN: 0927-796X. DOI: 10.1016/J.MSER.2020.100590.

[4] P. Pradhan and D. Singh, "Review on air suspension system," *Materials Today: Proceedings*, Apr. 2021, ISSN: 2214-7853. DOI: 10.1016/J.MATPR.2021.03.640.

[5] VDL Weweler-Colaert, *Trailing arm*. [Online]. Available: https://www.vdlweweler.nl/products/airsuspension.

[6] C. Chen, Z. Jiang, Y. Li, M. Sun, Q. Wang, K. Chen, and H. Li, "State of the Art in the Control of Inclusions in Spring Steel for Automobile - a Review," *ISIJ International*, vol. 60, no. 4, pp. 617–627, Apr. 2020, ISSN: 0915-1559. DOI: 10.2355/isijinternational.ISIJINT-2019-513.

[7] Yoshiro Yamada and Toshio Kuwabara, *Materials for Springs*. Berlin, Heidelberg: Springer Berlin Heidelberg, 2007, ISBN: 978-3-540-73811-4. DOI: 10.1007/978-3-540-73812-1.

[8] Z. Changle, F. Hanguang, M. Shengqiang, Y. Dawei, L. Jian, X. Zhenguo, and L. Yongping, "Effect of Mn content on microstructure and properties of wear-resistant bainitic steel," *Materials Research Express*, vol. 6, no. 8, p. 086 581, May 2019, ISSN: 2053-1591. DOI: 10.1088/2053-1591/ab1c8d.

[9] C. Goulas, M. G. Mecozzi, and J. Sietsma, "Bainite Formation in Medium-Carbon Low-Silicon Spring Steels Accounting for Chemical Segregation," *Metallurgical and Materials Transactions A*, vol. 47, no. 6, pp. 3077–3087, Jun. 2016, ISSN: 1073-5623. DOI: 10.1007/s11661-016-3418-6.

[10] H. Bhadeshia and R. Honeycombe, "Bainite," in *Steels: Microstructure and Properties*, Elsevier, 2017, pp. 179–202. DOI: 10.1016/b978-0-08-100270-4.00006-8.

[11] J. Wang, P. J. Van Der Wolk, and S. Van Der Zwaag, "On the influence of alloying elements on the bainite reaction in low alloy steels during continuous cooling," *Journal of Materials Science*, vol. 35, no. 17, pp. 4393–4404, 2000, ISSN: 00222461. DOI: 10.1023/A:1004865209116.

[12] Virgamet, *Alloy and Carbon Spring Steel*. [Online]. Available: https://virgamet.com/construction-alloy-and-carbon-spring-steel.

[13] K. Ibrahim and A. Ismail, "Influence of hot deformation and austempering process on microstructure and mechanical properties of high Si-Mn steel," *Canadian Metallurgical Quarterly*, vol. 44, no. 4, pp. 489–494, 2005. DOI: 10.1179/cmq.2005.44.4.489.

[14] K. Chen, Z. Jiang, F. Liu, J. Yu, Y. Li, W. Gong, and C. Chen, "Effect of quenching and tempering temperature on microstructure and tensile properties of microalloyed ultra-high strength suspension spring steel," *Materials Science and Engineering: A*, vol. 766, p. 138 272, Oct. 2019, ISSN: 0921-5093. DOI: 10.1016/J.MSEA.2019.138272.

[15] K. Chen, Z. Jiang, F. Liu, B. Zhao, H. Li, X. Ma, C. Kang, and Y. Li, "Enhanced mechanical properties by retained aust.enite in medium–carbon Si-rich microalloyed steel treated by quenching–tempering, austempering and austempering–tempering processes," *Materials Science and Engineering: A*, vol. 790, p. 139 742, Jul. 2020, ISSN: 0921-5093. DOI: 10.1016/J.MSEA.2020.139742.

[16] J. A. da Cruz, T. F. M. Rodrigues, V. D. C. Viana, and D. B. Santos, "Bainite Formation at Low Temperatures in High C-Si Steel and its Mechanical Behavior," *Materials Science Forum*, vol. 706-709, pp. 173–180, Jan. 2012, ISSN: 1662-9752. DOI: 10.4028/www.scientific.net/MSF.706-709.173.

[17] S. H. Kim, K.-H. Kim, C.-M. Bae, J. S. Lee, and D.-W. Suh, "Microstructure and Mechanical Properties of Austempered Medium-Carbon Spring Steel," *Metals and Materials International*, vol. 24, no. 4, pp. 693–701, Jul. 2018, ISSN: 1598-9623. DOI: 10.1007/s12540-018-0085-8.

[18] H. Aaronson, *The mechanism of phase transformation in crystalline solids*. London: Institute of Metals, 1969, pp. 270–280.

[19] M. Ohring, "How engineering materials are strengthened and toughened," *Engineering Materials Science*, pp. 431–500, Jan. 1995. DOI: 10.1016/B978-012524995-9/50033-7.

[20] H. K. D. H. Bhadeshia, *Bainite in Steels : Theory and Practice, Third Edition*, 3rd ed. Leeds: Chapman and Hall/CRC, 2019, ISBN: 9781351574815. [Online]. Available: https://public.ebookcentral.proquest.com/choice/publicfullrecord.aspx?p=5751773..

[21] F. G. Caballero, H. K. D. H. Bhadeshia, K. J. A. Mawella, D. G. Jones, and P. Brown, "Very strong low temperature bainite," *Materials Science and Technology*, vol. 18, no. 3, pp. 279–284, Mar. 2002, ISSN: 0267-0836. DOI: 10.1179/026708301225000725.

[22] A. M. Ravi, J. Sietsma, and M. J. Santofimia, "Exploring bainite formation kinetics distinguishing grain-boundary and autocatalytic nucleation in high and low-Si steels," *Acta Materialia*, vol. 105, pp. 155–164, Feb. 2016, ISSN: 1359-6454. DOI: 10.1016/J.ACTAMAT.2015.11.044.

[23] W. Pei, W. Liu, Y. Zhang, R. Qie, and A. Zhao, "Study on Kinetics of Transformation in Medium Carbon Steel Bainite at Different Isothermal Temperatures," *Materials*, vol. 14, no. 11, p. 2721, May 2021, ISSN: 1996-1944. DOI: 10.3390/ma14112721.

[24] J. Zhao, X. Zhao, X. Zhao, C. Dong, and S. Kang, "Effects of nucleation site and morphology of carbide-free bainite on microstructures and properties of bainite/martensite multi-phase steels," *Materials Science and Engineering: A*, vol. 744, pp. 86–93, Jan. 2019, ISSN: 0921-5093. DOI: 10.1016/J.MSEA.2018.11.060.

[25] S. Lin, A. Borgenstam, A. Stark, and P. Hedström, "Effect of Si on bainitic transformation kinetics in steels explained by carbon partitioning, carbide formation, dislocation densities, and thermodynamic conditions," *Materials Characterization*, vol. 185, p. 111 774, Mar. 2022, ISSN: 1044-5803. DOI: 10.1016/J.MATCHAR.2022.111774. [Online]. Available: https://linkinghub.elsevier.com/retrieve/pii/S1044580322000560.

[26] A. Lindstrom, "Austempered High Silicon Steel," Lulea University of Technology, Tech. Rep., 2006.

[27] R. Ranjan and S. B. Singh, "Isothermal bainite transformation in low-alloy steels: Mechanism of transformation," *Acta Materialia*, vol. 202, pp. 302–316, Jan. 2021, ISSN: 1359-6454. DOI: 10.1016/J.ACTAMAT.2020.10.048.

[28] F. G. Caballero, C. Garcia-Mateo, M. J. Santofimia, M. K. Miller, and C. García de Andrés, "New experimental evidence on the incomplete transformation phenomenon in steel," *Acta Materialia*, vol. 57, no. 1, pp. 8–17, Jan. 2009, ISSN: 1359-6454. DOI: 10.1016/J.ACTAMAT.2008.08.041.

[29] M. Hillert, L. Höglund, and J. Ågren, "Role of carbon and alloying elements in the formation of bainitic ferrite," *Metallurgical and Materials Transactions A: Physical Metallurgy and Materials Science*, vol. 35 A, no. 12, pp. 3693–3700, 2004. DOI: 10.1007/s11661-004-0275-5.

[30] H. I. Aaronson, W. T. Reynolds, and G. R. Purdy, "Coupled-solute drag effects on ferrite formation in Fe-C-X systems," *Metallurgical and Materials Transactions A*, vol. 35, no. 4, pp. 1187–1210, Apr. 2004, ISSN: 1073-5623. DOI: 10.1007/s11661-004-0294-2.

[31] Y. Li and X. Chen, "Microstructure and mechanical properties of austempered high silicon cast steel," *Materials Science and Engineering: A*, vol. 308, no. 1-2, pp. 277–282, Jun. 2001, ISSN: 09215093. DOI: 10.1016/S0921-5093(00)01779-2.

[32] D. Mandal, M. Ghosh, J. Pal, P. K. De, S. Ghosh Chowdhury, S. K. Das, G. Das, and S. Ghosh, "Effect of austempering treatment on microstructure and mechanical properties of high-Si steel," *Journal of Materials Science*, vol. 44, no. 4, pp. 1069–1075, Feb. 2009, ISSN: 0022-2461. DOI: 10.1007/s10853-008-3203-z.

[33] S. K. Putatunda, A. V. Singar, R. Tackett, and G. Lawes, "Development of a high strength high toughness ausferritic steel," *Materials Science and Engineering A*, vol. 513-514, no. C, pp. 329–339, Jul. 2009, ISSN: 09215093. DOI: 10.1016/j.msea.2009.02.013.

[34] F. G. Caballero, H. K. D. H. Bhadeshia, K. J. A. Mawella, D. G. Jones, and P. Brown, "Very strong low temperature bainite," *Materials Science and Technology*, vol. 18, no. 3, pp. 279–284, Mar. 2002, ISSN: 0267-0836. DOI: 10.1179/026708301225000725.

[35] C. Hofer, V. Bliznuk, A. Verdiere, R. Petrov, F. Winkelhofer, H. Clemens, and S. Primig, "High-resolution characterization of the martensite-austenite constituent in a carbide-free bainitic steel," *Materials Characterization*, vol. 144, pp. 182–190, Oct. 2018, ISSN: 1044-5803. DOI: 10.1016/J.MATCHAR.2018.07.011.

[36] B. Buchmayr, "Critical assessment 22: Bainitic forging steels," *Materials Science and Technology (United Kingdom)*, vol. 32, no. 6, pp. 517–522, 2016. DOI: 10.1080/02670836.2015.1114272.

[37] T. Suzuki, Y. Ono, G. Miyamoto, and T. Furuhara, "Effects of Si and Cr on Bainite Microstructure of Medium Carbon Steels," *ISIJ International*, vol. 50, no. 10, pp. 1476–1482, 2010, ISSN: 0915-1559. DOI: 10.2355/isijinternational.50.1476.

[38] A. Varshney, S. Sangal, A. K. Pramanick, and K. Mondal, "On the extent of transformation of austenite to bainitic ferrite and carbide during austempering of high Si steel for prolonged duration and its effect on mechanical properties," *Materials Science and Engineering: A*, vol. 793, p. 139 764, Aug. 2020, ISSN: 0921-5093. DOI: 10.1016/J.MSEA.2020.139764.

[39] P. Acharya, A. Kumar, and R. Bhat, "Microstructure and wear behavior of austempered high carbon high silicon steel," *MATEC Web of Conferences*, vol. 144, p. 02 013, Jan. 2018, ISSN: 2261-236X. DOI: 10.1051/matecconf/201714402013.

[40] P. A. Palaksha and K. S. Ravishankar, "Influence of Austempering Heat Treatment on Microstructure and Mechanical Properties of Medium Carbon High Silicon Steel," *IOP Conference Series: Materials Science and Engineering*, vol. 225, p. 012 006, Aug. 2017, ISSN: 1757-8981. DOI: 10.1088/1757-899X/225/1/012006.

[41] I. B. Timokhina, K. D. Liss, D. Raabe, K. Rakha, H. Beladi, X. Y. Xiong, and P. D. Hodgson, "Growth of bainitic ferrite and carbon partitioning during the early stages of bainite transformation in a 2mass% silicon steel studied by in situ neutron diffraction, TEM and APT," *Journal of Applied Crystallography*, vol. 49, no. 2, pp. 399–414, Apr. 2016, ISSN: 1600-5767. DOI: 10.1107/S1600576716000418.

[42] A. Królicka, K. Radwański, A. Ambroziak, and A. Żak, "Analysis of grain growth and morphology of bainite in medium-carbon spring steel," *Materials Science and Engineering: A*, vol. 768, p. 138 446, Dec. 2019, ISSN: 09215093. DOI: 10.1016/j.msea.2019.138446.

[43] C. Hofer, F. Winkelhofer, H. Clemens, and S. Primig, "Morphology change of retained austenite during austempering of carbide-free bainitic steel," *Materials Science and Engineering: A*, vol. 664, pp. 236–246, May 2016, ISSN: 0921-5093. DOI: 10.1016/J.MSEA.2016.04.005.

[44] C. Hofer, S. Primig, H. Clemens, F. Winkelhofer, and R. Schnitzer, "Influence of Heat Treatment on Microstructure Stability and Mechanical Properties of a Carbide-Free Bainitic Steel," *Advanced Engineering Materials*, vol. 19, no. 4, pp. 1–12, Apr. 2017, ISSN: 14381656. DOI: 10.1002/adem.201600658.

[45] Ö. Murathan, V. Kilicli, and K. Davut, "Effect of Austempering Heat Treatments on Microstructure and Mechanical Properties of AISI 9254 Commercial Spring Steel," Apr. 2015.

[46] K. Chen, H. Li, Z. Jiang, F. Liu, C. Kang, X. Ma, and B. Zhao, "Multiphase microstructure formation and its effect on fracture behavior of medium carbon high silicon high strength steel," *Journal of Materials Science & Technology*, vol. 72, pp. 81–92, May 2021, ISSN: 1005-0302. DOI: 10.1016/J.JMST.2020.09.034.

[47] S. M. Hasan, S. Kumar, D. Chakrabarti, and S. B. Singh, "Effect of prior austenite grain size on the formation of carbide-free bainite in low-alloy steel," *Philosophical Magazine*, vol. 100, no. 18, pp. 2320–2334, Sep. 2020, ISSN: 1478-6435. DOI: 10.1080/14786435.2020.1764653.

[48] R. Ueji, Y. Kimura, K. Ushioda, T. Ohmura, and T. Inoue, "Bainite Transformation and Resultant Tensile Properties of 0.6%C Low Alloyed Steels with Different Prior Austenite Grain Sizes," *ISIJ International*, vol. 61, no. 2, pp. 582–590, Feb. 2021, ISSN: 0915-1559. DOI: 10.2355/isijinternational.ISIJINT-2020-389.

[49] V. Wirths, W. Bleck, R. Wagener, and T. Melz, "Carbide free bainitic forging steels with improved fatigue properties," Oct. 2015.

[50] C. Liu, Y. Chen, C. Zhang, D. Chen, and G. Cui, "Enhanced strength and plasticity in a novel 55Si2MnMoV spring steel via austempering," *Materials Science and Engineering: A*, vol. 825, p. 141 887, Sep. 2021, ISSN: 0921-5093. DOI: 10.1016/J.MSEA.2021.141887.

[51] J.-C. Hell, M. Dehmas, S. Allain, J. M. Prado, A. Hazotte, and J.-P. Chateau, "Microstructure – Properties Relationships in Carbide-free Bainitic Steels," *ISIJ International*, vol. 51, no. 10, pp. 1724–1732, 2011, ISSN: 0915-1559. DOI: 10.2355/isijinternational.51.1724.

[52] B. R. Shendy, M. N. Yoozbashi, B. Avishan, and S. Yazdani, "An Investigation on Rotating Bending Fatigue Behavior of Nanostructured Low-Temperature Bainitic Steel," *Acta Metallurgica Sinica (English Letters)*, vol. 27, no. 2, pp. 233–238, Apr. 2014, ISSN: 1006-7191. DOI: 10.1007/s40195-014-0044-4.

[53] K. Zhu, H. Chen, J. P. Masse, O. Bouaziz, and G. Gachet, "The effect of prior ferrite formation on bainite and martensite transformation kinetics in advanced high-strength steels," *Acta Materialia*, vol. 61, no. 16, pp. 6025–6036, Sep. 2013, ISSN: 1359-6454. DOI: 10.1016/J.ACTAMAT.2013.06.043.

[54] S. Slama, M. Bouhafs, J. Bessrour, M. Ben Jaber, and H. Mokdadi, "Numerical simulation of heat transfer during leaf spring industrial quenching process," *Mechanics & Industry*, vol. 19, no. 3, p. 304, Sep. 2018, ISSN: 2257-7777. DOI: 10.1051/meca/2018013.

[55] M. Ackermann, B. Resiak, P. Buessler, B. Michaut, and W. Bleck, "Effect of Molybdenum and Cooling Regime on Microstructural Heterogeneity in Bainitic Steel Wires," *steel research international*, vol. 91, no. 11, p. 1 900 663, Nov. 2020, ISSN: 1611-3683. DOI: 10.1002/srin.201900663.

[56] A. Basso, A. Eres-Castellanos, N. Tenaglia, D. San-Martin, J. Jimenez, and F. Caballero, "Effect of microsegregation and bainitic reaction temperature on the microstructure and mechanical properties of a high-carbon and high-silicon cast steel," *Metals*, vol. 11, no. 2, pp. 1–31, 2021. DOI: 10.3390/met11020220.

[57] A. D. Basso, I. Toda-Caraballo, A. Eres-Castellanos, D. San-Martin, J. A. Jimenez, and F. G. Caballero, "Effect of the Microsegregation on Martensitic and Bainitic Reactions in a High Carbon-High Silicon Cast Steel," *Metals*, vol. 10, no. 5, p. 574, Apr. 2020, ISSN: 2075-4701. DOI: 10.3390/met10050574.

[58] F. Caballero, "Carbide-free bainite in steels," in *Phase Transformations in Steels*, Elsevier, 2012, pp. 436–467. DOI: 10.1533/9780857096104.3.436.

[59] F. Caballero, M. Miller, C. Garcia-Mateo, C. Capdevila, and S. Babu, "Redistribution of alloying elements during tempering of a nanocrystalline steel," *Acta Materialia*, vol. 56, no. 2, pp. 188–199, Jan. 2008, ISSN: 13596454. DOI: 10.1016/j.actamat.2007.09.018.

[60] G. Gao, H. Zhang, X. Gui, Z. Tan, B. Bai, and Y. Weng, "Enhanced strain hardening capacity in a lean alloy steel treated by a "disturbed" bainitic austempering process," *Acta Materialia*, vol. 101, pp. 31–39, Dec. 2015, ISSN: 1359-6454. DOI: 10.1016/J.ACTAMAT.2015.08.071.

[61] "Standard Practice for Microetching Metals and Alloys 1," Tech. Rep. [Online]. Available: www.astm.org.

[62] ASTM E976-13., "Standard Practice for X-Ray Determination of Retained Austenite in Steel with Near Random Crystallographic Orientation 1," *ASTM International*, 2013. DOI: 10.1520/E0975-13. [Online]. Available: http://www.sae.org..

[63] N. van Dijk, A. Butt, L. Zhao, J. Sietsma, S. Offerman, J. Wright, and S. Vanderzwaag, "Thermal stability of retained austenite in TRIP steels studied by synchrotron X-ray diffraction during cooling," *Acta Materialia*, vol. 53, no. 20, pp. 5439–5447, Dec. 2005, ISSN: 13596454. DOI: 10.1016/j.actamat.2005.08.017.

[64] C. F. Jatczak, "Retained Austenite and Its Measurement by X-Ray Diffraction," Feb. 1980. DOI: 10.4271/800426.

[65] C. Hofer, F. Winkelhofer, J. Krammerbauer, H. Clemens, and S. Primig, "Atom Probe Tomography of Carbides Occurring in "Carbide-free" Bainitic Steels," *Materials Today: Proceedings*, vol. 2, S925–S928, Jan. 2015, ISSN: 2214-7853. DOI: 10.1016/J.MATPR.2015.07.433.

[66] J. Tian, G. Xu, Z. Jiang, X. Wan, H. Hu, and Q. Yuan, "Transformation Behavior and Properties of Carbide-Free Bainite Steels with Different Si Contents," *steel research international*, vol. 90, no. 3, p. 1 800 474, Mar. 2019, ISSN: 16113683. DOI: 10.1002/srin.201800474.

[67] Y. Tian, Z. Tan, H. Li, B. Gao, J. Zhu, Y. Liu, and M. Zhang, "A new finite element model for Mn-Si-Cr bainitic/martensitic product quenching process: Simulation and experimental validation," *Journal of Materials Processing Technology*, vol. 294, p. 117 137, Aug. 2021, ISSN: 0924-0136. DOI: 10.1016/J.JMATPROTEC.2021.117137.

[68] H. Matsuda, R. Mizuno, Y. Funakawa, K. Seto, S. Matsuoka, and Y. Tanaka, "Effects of auto-tempering behaviour of martensite on mechanical properties of ultra high strength steel sheets," *Journal of Alloys and Compounds*, vol. 577, S661–S667, Nov. 2013, ISSN: 09258388. DOI: 10.1016/j.jallcom.2012.04.108.

[69] H. Bhadeshia, "A rationalisation of shear transformations in steels," *Acta Metallurgica*, vol. 29, no. 6, pp. 1117–1130, Jun. 1981, ISSN: 00016160. DOI: 10.1016/0001-6160(81)90063-8.

[70] N. E. Tenaglia, A. L. Rivas, R. E. Boeri, J. M. Massone, and A. D. Basso, "Study of austempering kinetics of high silicon bainitic cast steels," *International Journal of Cast Metals Research*, vol. 32, no. 1, pp. 21–30, Jan. 2019, ISSN: 1364-0461. DOI: 10.1080/13640461.2018.1505423.

[71] L. Morales-Rivas, H. Roelofs, S. Hasler, C. García-Mateo, and F. G. Caballero, "Complex Microstructural Banding of Continuously Cooled Carbide-Free Bainitic Steels," *Materials Science Forum*, vol. 783-786, pp. 980–985, May 2014, ISSN: 1662-9752. DOI: 10.4028/www.scientific.net/MSF.783-786.980.

[72] J. Ågren, "A revised expression for the diffusivity of carbon in binary FeC austenite," *Scripta Metallurgica*, vol. 20, no. 11, pp. 1507–1510, Nov. 1986, ISSN: 00369748. DOI: 10.1016/0036-9748(86)90384-4.

[73] J. Chiang, B. Lawrence, J. D. Boyd, and A. K. Pilkey, "Effect of microstructure on retained austenite stability and work hardening of TRIP steels," *Materials Science and Engineering: A*, vol. 528, no. 13-14, pp. 4516–4521, May 2011, ISSN: 0921-5093. DOI: 10.1016/J.MSEA.2011.02.032.

[74] S. M. Hasan, A. Mandal, S. B. Singh, and D. Chakrabarti, "Work hardening behaviour and damage mechanisms in carbide-free bainitic steel during uni-axial tensile deformation," *Materials Science and Engineering: A*, vol. 751, pp. 142–153, Mar. 2019, ISSN: 09215093. DOI: 10.1016/j.msea.2019.02.062.

A

APPENDIX-A

Figure A.1 displays the distribution of carbon in each phase. At low temperatures (under 340^oC), M_7C_3 carbides present high carbon content and carbon is distributed also, in M_3C_2 carbides. These two phases are rich in manganese and chromium respectively. At higher temperatures, cementite and austenite contain most of the carbon.

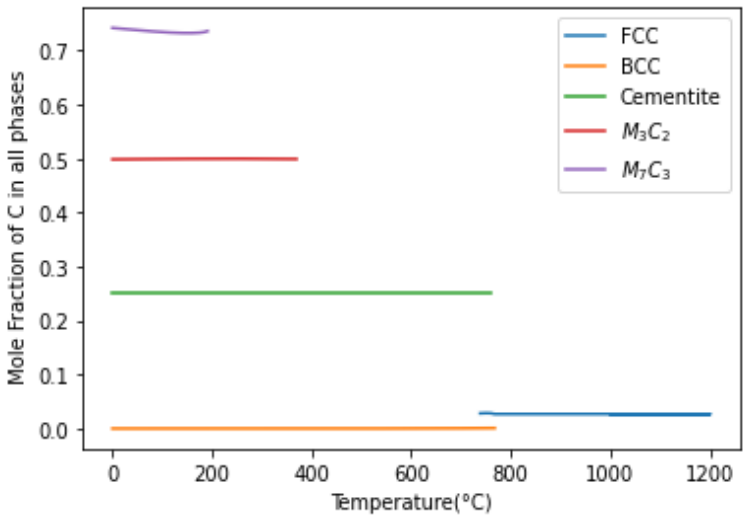

Figure A.1: Mol fraction of carbon in all phases versus temperature for 61SiCr7 using Thermo-Calc software.

In figure A.2, the CCT diagram of the nominal composition is presented.

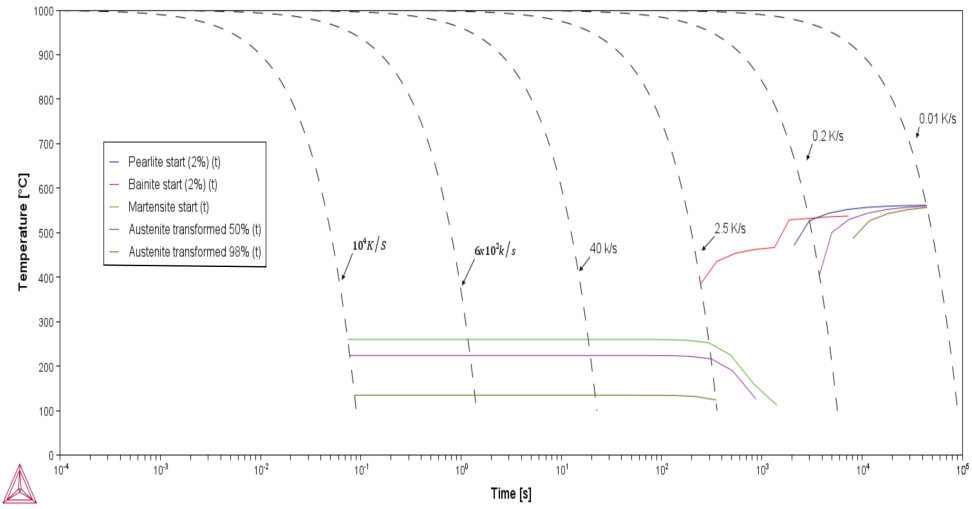

Figure A.2: Continuous cooling transformation (CCT) of base composition of Fe-0.60C-1.63Si-0.97Mn-0.48Cr using Thermo-Calc software.

Bainite is expected to be formed during austempering for slow cooling rates (≤2.5 K/s) as the martensitic transformation will be suppressed as the bainitic transformation progresses.

A.1. MICROSTRUCTURE OF THE BACK PART

Figure A.3 (a-e) shows the micrographs after optical microscopy and SEM of the B1 surface of steel specimens from lower to higher magnifications. Bainitic ferrite, M-A islands and carbides were indicated.

The B3 surface of spring steel is presented in figure A.4. Microstructural bands were observed close to the surface of the sample perpendicular to the rolling direction. Figure A.4 (b) displays the decarburized layer which is usually present in industrially produced components. M-A islands were also identified. Moreover, a grain size variation was observed between the banded and non-banded structures. More specifically, the banded area indicated by black arrows,in figure A.4 (a) demonstrated coarser grain size.

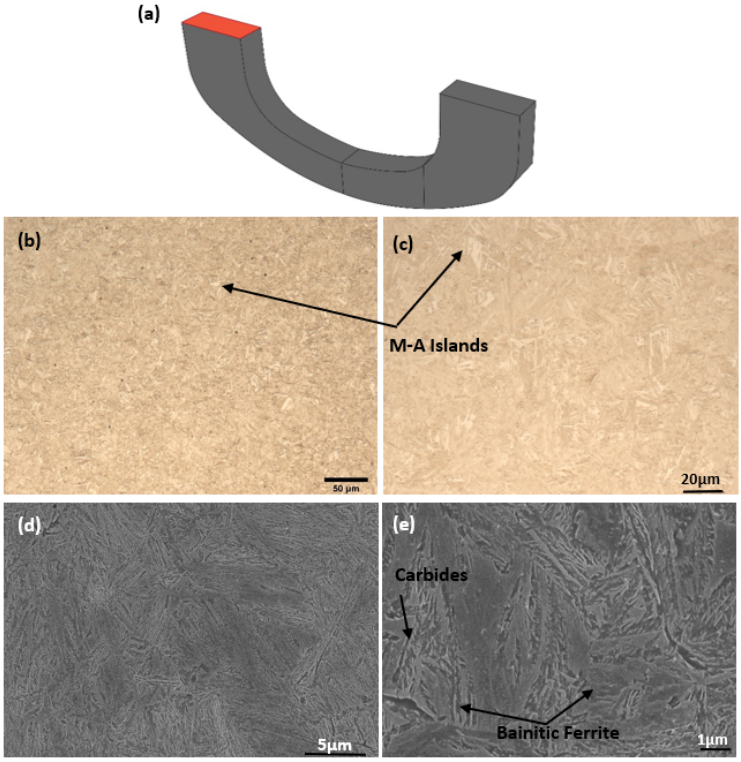

Figure A.3: (a) Location of B1 surface on the back part of trailing arm, (b),(c) optical and (d),(e) SEM micrographs of B1 surface of 61SiCr7 steel after austempering for 1 hour from lower to higher magnification. Bainitic ferrite, carbides, and M-A islands are indicated.

A

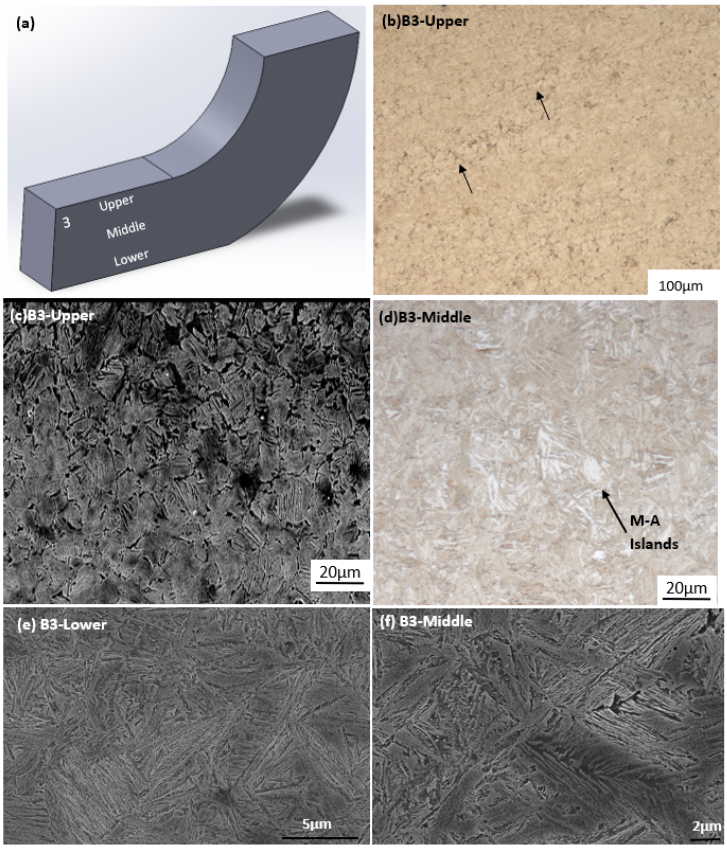

Figure A.4: (a)Location of the investigated surface (b),(c),(d) Optical and (e),(f) SEM micrographs of austempered 61SiCr7 of B3 area. Coarser grains in banded structure and M-A islands are indicated in black arrows.

B

APPENDIX-B

This section indicates how the results could be used in the investigation and analysis of microstructural inhomogeneity in different scales in silicon steels used in engineering applications such as pipe and bearing steels. In these steels, the production of this microstructure presents challenges also, due to also thermal gradient, chemical segregation and carbon gradient. In that way, a scientific basis and a design could be created to explain microstructural inhomogeneity in different scales to obtain a carbide-free bainitic microstructure in steels in large-scale applications.

B.1. INVESTIGATION OF MICROSTRUCTURAL HETEROGENEITY IN DIFFERENT SCALES IN SILICON STEELS

B.1.1. INTRODUCTION

Bainite's formation in the automotive industry has grown great interest over the last years as simultaneously features such as high strength and the transformation- induced plasticity (TRIP) effect could be combined. More specifically, studies have been conducted that carbide-free bainite (austenitic microstructure) which consists of bainitic ferrite and enriched austenite with carbon at room temperature could achieve high tensile and fatigue properties. This microstructure is achieved by the addition of silicon (over 1.5 wt.%) and the application of austempering (isothermal heat treatment). However, processing routes (rolling, forging, cooling rate) and austempering temperature and time could affect this microstructure and influence accordingly material's mechanical properties. In this work, microstructural inhomogeneity could be explained in different scales

B.1.2. EXPERIMENTAL METHODS

Microstructural distribution was investigated of silicon steel (Fe-0.6C-1.63Si-0.97Mn-0.48Cr) after austempering for 1 hour at M_s+50^{o}C. Three reasons: thermal gradient, chemical segregation, and carbon gradient were indicated to explain possible microstruc-

tural heterogeneity in different scales using optical microscopy, scanning electron microscopy (SEM), electron probe micro analysis (EPMA), X-ray diffraction (XRD), and hardness measurements. These reasons were opted for based on the heat treatment applied and the chemical composition of the steel.

B.1.3. RESULTS-DISCUSSION

The results gave insights into the effect of the processing route on the microstructure. Bainitic ferrite together with martensitic-austenitic islands, and carbide particles were the main microstructural features instead of an ausferritic microstructure.

Segregation bands formed parallel to the rolling direction rich in Si, Mn, and Cr and were confirmed from optical microscopy, SEM, and EPMA. In regions with high concentrations of substitutional elements, the bainitic transformation was delayed. Furthermore, on the surface of the steel which had a low amount of retained austenite (8%), the bainitic transformation was ceased based on the To curve (austenite reached a specific carbon content over which bainitic transformation based on the diffusionless theory is not possible). The identification also, of auto-tempered martensitic-austenitic islands (carbides precipitating in M-A islands) lead to the conclusion that both thermal and carbon gradients were present. These three reasons result in non-uniform bainitic nucleation and growth.

B.1.4. CONCLUSION

The design of processing route heat treatment in this type of steel plays a significant role in the final microstructure as all three reasons were confirmed. Furthermore, austempering parameters and chemical composition should be selected cautiously to achieve the desired microstructure.